

# INVESTIGATION OF LOCAL BREAKDOWN OF THE QUANTUM HALL EFFECT IN GRAPHENE PROBED WITH INVASIVE METAL CONTACTS

BY FABIAN DUERR

A thesis submitted to the  
Graduate School—New Brunswick  
Rutgers, The State University of New Jersey  
in partial fulfillment of the requirements  
for the degree of  
Master of Science  
Graduate Program in Physics and Astronomy

Written under the direction of  
Prof. Eva Andrei  
and approved by

---

---

---

New Brunswick, New Jersey

October, 2009

## **ABSTRACT OF THE THESIS**

# **Investigation of local breakdown of the Quantum Hall Effect in graphene probed with invasive metal contacts**

**by Fabian Duerr**

**Thesis Director: Prof. Eva Andrei**

We investigate the local breakdown of the Quantum Hall Effect (QHE) effect in a graphene device caused by the constraints of the Hall bar geometry and finite size of the sample. First to account for principal features of the data we use a multi-carrier model that simulates the transverse and longitudinal resistance of doped samples in low magnetic fields. This model however can not reproduce the reduction of Hall voltage measured in the vicinity of the current leads. Therefore we introduce a second model which describes the effect of distribution of electric field in the device, giving a reasonable scenario that can explain our experimental data and deviations from the case of perfect geometry. We conclude that the existence of Hot Spots in two corners of the sample leads to the local break down of the QHE around this points.

## Acknowledgements

First I want to thank the people who made all this possible. Prof. Fakher Assaad from the University of Würzburg for organizing this excellent program, the Deutscher Akademischer Austauschdienst DAAD for the financial support. Prof. Ronald Ransome and Shirley Hinds who did such a great job in making my stay as uncomplicated as possible. Thanks a lot.

I'm deeply thankful to my advisor Prof. Eva Andrei for all fruitful discussions and for accomodating me in such a great group. I want to thank Xu Du for introducing me in the facinating world of graphene. I'm sure you will do great at Stony Brook. Thanks to Adina, Guhong Lee, Patrick and Justin, for helping me whenever it was needed. I want to express my deep gratitude to Ivan Skachko for teaching me so much, for always having time for small discussion, and in particularly for spending so much time helping me with my work. This would not have been possible without you. Thanks to Prof. Dmitry Abanin from Princeton Univeristy for providing us with helpful calculations.

I want to thank all my friends I found here in the States for making the stay so incredible enjoyable and of course Gunnar and Heiko for sharing this great experience with me.

## Dedication

*To my family*

# Table of Contents

<b>Abstract</b> . . . . .	ii
<b>Acknowledgements</b> . . . . .	iii
<b>Dedication</b> . . . . .	iv
<b>List of Tables</b> . . . . .	vii
<b>List of Figures</b> . . . . .	viii
<b>1. Background</b> . . . . .	1
1.1. Introduction . . . . .	1
1.2. Atomic structure . . . . .	4
1.3. Tight-binding model for graphene . . . . .	6
1.4. Density of states . . . . .	11
1.5. Electron hole puddles and scatterers in graphene . . . . .	12
1.6. Influence of metal contacts . . . . .	14
1.7. Magnetotransport . . . . .	18
1.7.1. Classical Hall Effect . . . . .	18
1.7.2. Multi-band model . . . . .	21
1.8. Quantum Hall effect in graphene . . . . .	27
1.9. Edge states . . . . .	31
<b>2. Experiment</b> . . . . .	33
2.1. Sample Preparation . . . . .	33
2.2. Electron Beam Lithography . . . . .	34
2.3. Electron Beam Evaporation . . . . .	38
2.4. Experimental setup . . . . .	40

<b>3. Data analysis</b> . . . . .	45
3.1. Sample characterization . . . . .	45
3.2. Hall measurement . . . . .	50
3.3. Potential distribution in a Hall bar . . . . .	54
3.3.1. Infinite contact resistance . . . . .	57
3.3.2. Vanishing contact resistance . . . . .	58
3.3.3. Finite contact resistance . . . . .	59
3.3.4. Summary and Outlook . . . . .	62
<b>References</b> . . . . .	65

## List of Tables

2.1. E-beam lithography parameters . . . . .	36
2.2. Metal deposition parameters . . . . .	39
3.1. Dimensions (see Fig.2.4) of samples S1, S2 and S3. Since S1 has three voltage pairs, it has two corresponding $L_{HL}$ 's and $\Delta$ 's . . . . .	45
3.2. Parameters extracted from transport measurement. . . . .	49

## List of Figures

1.1. Suspended graphene sample . . . . .	2
1.2. Carbon allotropes . . . . .	4
1.3. Real space and reciprocal space lattices of two dimensional carbon . . . . .	5
1.4. Energy dispersion of graphene . . . . .	8
1.5. Chirality in graphene . . . . .	10
1.6. DOS of a 2DEG and graphene . . . . .	12
1.7. Potential fluctuations in graphene . . . . .	13
1.8. Metal/graphene interface . . . . .	15
1.9. Contact induced states in graphene . . . . .	16
1.10. Classical Hall effect . . . . .	20
1.11. Influence of p-type doping on Hall resistance ( $B=1T$ ) . . . . .	23
1.12. Influence of electron hole puddles on Hall Resistance ( $B=1T$ ) . . . . .	23
1.13. Influence of the mobility of the charge carriers in the impurity state on Hall resistance ( $B=1T$ ) . . . . .	24
1.14. Density of states for hole doped graphene . . . . .	25
1.15. Influence of a second p-type dopant on the Hall resistance ( $B=1T$ ) . . . . .	26
1.16. DOS of graphene in magnetic field . . . . .	28
1.17. QHE in graphene . . . . .	30
1.18. Edge states in graphene . . . . .	31
2.1. Graphite on substrate . . . . .	34
2.2. E-beam lithography . . . . .	35
2.3. Electron beam hitting resist and substrate . . . . .	35
2.4. Sample geometry/design . . . . .	37
2.5. E-beam evaporation system . . . . .	38



2.6. Summary of preparation process . . . . .	40
2.7. Experimental setup . . . . .	41
2.8. Measurement circuit . . . . .	42
2.9. Schematic setup . . . . .	43
3.1. Resistivity $\rho_{xx}$ versus back gate voltage $V_G$ . . . . .	46
3.2. Estimation of puddle size $Z$ . . . . .	47
3.3. Conductivity $\sigma_{xx}$ versus back voltage $V_G$ . . . . .	47
3.4. Mobility $\mu$ versus back gate voltage . . . . .	48
3.5. Mean free path $l$ versus back gate voltage . . . . .	49
3.6. Optical image of typical Hall bar . . . . .	51
3.7. Hall resistance $R_H$ for sample S3 . . . . .	51
3.8. Hall resistance $R_H$ for sample S2 . . . . .	52
3.9. Fits for Hall resistance of S1 . . . . .	52
3.10. Sample S1 in low magnetic field . . . . .	53
3.11. Samples S1,S2 and S3 in high magnetic fields . . . . .	54
3.12. Hall angle of S1 . . . . .	55
3.13. Potential distribution in a Hall Bar . . . . .	56
3.14. Absolute value of electric field in a Hall Bar . . . . .	57
3.15. Hall resistance for voltage leads with infinite contact resistance . . . . .	58
3.16. Hall resistance for voltage leads with vanishing contact resistance . . . . .	59
3.17. Potential distribution for various contact resistances of the voltage leads . . . . .	61
3.18. Longitudinal resistance of S1 in 9 Tesla . . . . .	63

# Chapter 1

## Background

### 1.1 Introduction

Since graphene, a single layer of carbon atoms, was first discovered in 2004 [1] it is one of the hot topics in condensed matter physics, in experiment as well as in theory. According to the Mermin-Wagner theorem a two dimensional system should be unstable and does not exist in nature [2]. Indeed, it was always there, but one was not able to detect. However an accidental use of the silicon substrate having 300nm of oxide which results in constructive interference of light finally lead to the surprising discovery. A smallest disturbance, such as a single layer of carbon atoms, disrupts such interference and will make the graphene layer visible.

Prior to its' discovery the principal way to realize two dimensional systems was to confine electrons at the interface of GaAs/GaAlAs heterostructures or within Si MOS inversion layers. In contrast graphene is open to the environment and is therefore accessible to various scanning probes. It's unique linear band structure surely gains the most attention and leads to many exciting predictions. The carriers are described by the pseudo relativistic Dirac equation for massless fermions opening the door to probe quantum electro dynamical effects such as Klein paradoxon or Zitterbewegung on a table top experiment. Yet it is not only the the electrical properties that are making graphene so special, but also it's mechanical strength [3] and sensitivity to a small number of adsorbed molecules [4], making it interesting for various applications. An up-to-date review about the status and prospects of graphene can be found in Ref.[5] and about the electronic properties in Ref.[6].

The Quantum Hall effect in two dimensional electron gas (2DEG) systems [7] is a well studied phenomena and can also be observed in graphene[8], but with a rather unusual quantization of resistance. Similar to the 2DEGs one can achieve a high mobility of the

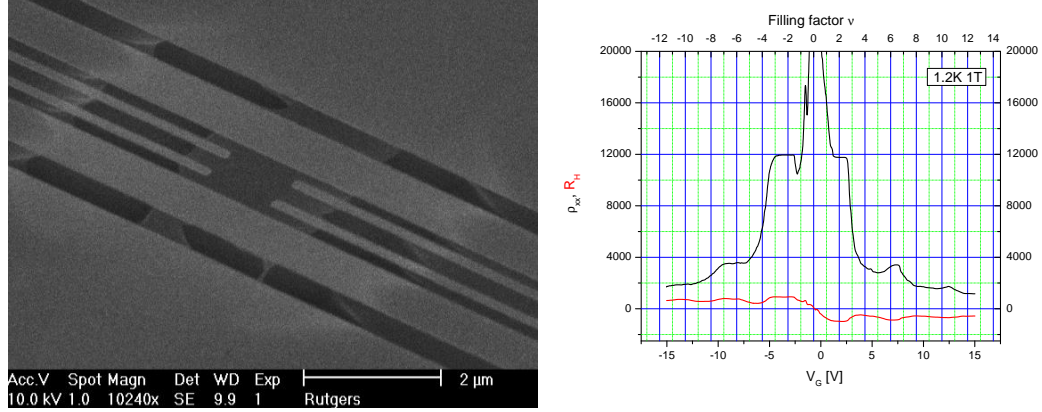


Figure 1.1: Suspended graphene sample. Left: SEM image of the suspended Hall bar sample. The sample is about  $2\mu m$  wide and  $1.5\mu m$  long. Right: Longitudinal and transverse resistivity  $\rho_{xx}$  and  $R_H$ . The longitudinal rather than the transverse resistance shows the expected quantized resistance for filling factors of  $\nu = 2, 6, 10, \dots$ , indicating a shorting of the voltage leads to the adjacent current leads.

charge carriers in graphene. The latter can be extremely improved by more than a factor of 10 by suspending graphene from the substrate [9, 10]. However, the quantum Hall effect in suspended graphene shows an unexpected behavior if the measurement is performed using standard Hall bar technique. The longitudinal resistance shows resistance plateaus that are expected for the Hall resistance, whereas the latter is very small and seems to be shorted to the current leads, as shown in Fig:1.1.

The motivation for this work was to investigate the effect of shorting of the voltage leads to the current leads. We proceed by trying to reproduce this result for non-suspended graphene and compare the Hall resistance measured at several locations along the sample's edge. We find that the Hall resistance is smaller close to the current leads, though the effect is weaker than in suspended graphene. Our first approach was to explain this behavior by a local doping effect of graphene by the metal electrodes [11], based on the inverse proportionality of the Hall resistance. For this purposed we adopted a simple multi-band model, that reproduces the longitudinal and transverse resistances for doped graphene in small magnetic fields. However, it does not explain the reduced Hall resistance close to the current leads.

Our second model, based on the pattern of electric field in a Hall bar, finally gives us the clue to solve this problem. The existence of so called hot spots [12, 13] at two corners of the

sample seems to be crucial to understand our data. All equipotential lines will accumulate in this two points and the entire power dissipation will happen there. For conventional 2DEGs the large size of samples allows placing the voltage leads sufficiently far away from those spots. But in graphene, particularly for its' suspended implementation, there is a limit of the sample length  $\leq 2\mu m$  by the requirement of its' mechanical stability. In addition the removal of the substrate and the heat sinking associated with it might make the Hot Spots a major issue.

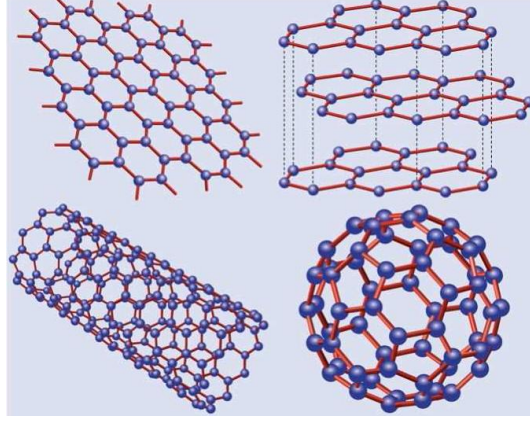


Figure 1.2: Carbon allotropes [6]. Top left: Carbon atoms are arranged in a honeycomb in-plane structure and form a single graphene layer. Top right: Shifted stacking of many single layers forms graphite. Bottom right: The Bucky ball ( $C_{60}$  fullerene) consists of 60 carbon atoms arranged in penta- and hexagons. Bottom left: Carbon nanotubes are rolled-up graphene sheets.

## 1.2 Atomic structure

Graphene is a two dimensional allotrope of carbon. Rolled-up it forms one dimensional carbon nanotubes which were extensively studied over the last two decades. Arranged in a spherical structure with 60 carbon atoms, sitting in a lattice formed by hexagons and pentagons, it is known as zero-dimensional  $C_{60}$  fullerene or Bucky ball. Stacked in different layers weakly coupled by Van der Waals forces it generates three dimensional graphite (see Fig.1.2). The carbon atoms in graphene are arranged in a highly symmetric honeycomb lattice. Neighboring atoms form a strong in-plane  $\sigma$ -bond with their s-orbital and three of their p-orbitals ( $sp^2$  hybridization). These orbitals are filled and represent a deeply laying valence band. The last valence electron is sitting in the unaffected p-orbital perpendicular orientated to the plane. Since there are two p-electrons per unit cell, containing two carbon atoms, those p-orbitals form a filled band that is of interest for the electronic properties of graphene.

The structure is described by two triangular lattices of atoms  $A$  and  $B$  shifted by  $\sqrt{3}a$ , where  $a \approx 0.142nm$  is the distance between neighboring carbon atoms (see Fig.1.3). The

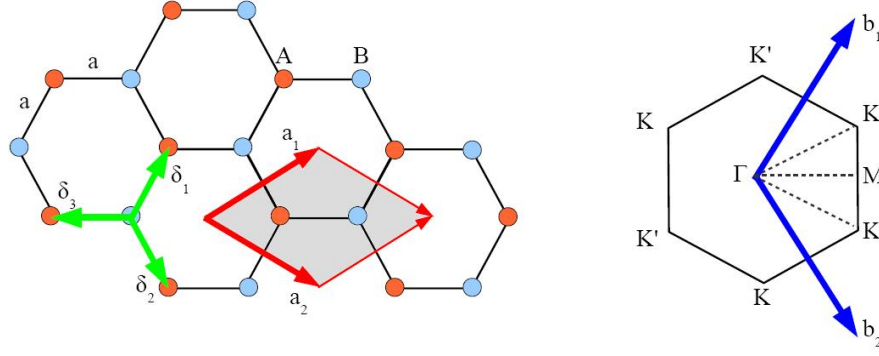


Figure 1.3: Real space and reciprocal space lattices of two dimensional carbon. Left: The crystal lattice of graphene is described by two triangular lattices formed by atoms  $A$  and  $B$  distanced by the lattice constant  $a \approx 0.142nm$ . Even though those atoms are chemically equal they have to be treated separately because of their bond orientation. The nearest neighbor vectors are described by  $\vec{\delta}_i$ . The unit cell (gray shaded) is spanned by the lattice vectors  $\vec{a}_i$ . Right: The corresponding Brillouin zone to the reciprocal lattice vectors  $\vec{b}_i$  is also represented by a honeycomb shape. It is restricted by the high symmetry  $K$ -points.

lattice vectors  $\vec{a}_1$  and  $\vec{a}_2$  form the unit cell containing two carbon atoms, one of each lattice site.

$$\vec{a}_1 = \frac{a}{2}(3, \sqrt{3}) \quad , \quad \vec{a}_2 = \frac{a}{2}(3, -\sqrt{3}) \quad (1.1)$$

The nearest neighbor vectors  $\delta_i$  are give by:

$$\delta_1 = \frac{a}{2}(1, \sqrt{3}), \quad \delta_2 = \frac{a}{2}(1, -\sqrt{3}), \quad \delta_3 = a(-1, 0) \quad (1.2)$$

The reciprocal lattice vectors are calculated to be:

$$\vec{b}_1 = (1, \sqrt{3}) \quad , \quad \vec{b}_2 = (-1, \sqrt{3}) \quad (1.3)$$

The corresponding Brillouin zone forms again a honeycomb lattice that is rotated by 90 degrees to the real space lattice. The high symmetry points in momentum space are denoted as  $K$  and  $K'$ . Their location is given by:

$$\vec{K} = \frac{2\pi}{a} \left( \frac{1}{3\sqrt{3}}, \frac{1}{3} \right) \quad , \quad \vec{K}' = \frac{2\pi}{a} \left( \frac{1}{3\sqrt{3}}, -\frac{1}{3} \right) \quad (1.4)$$

As the atoms  $A$  and  $B$  in real space, the so-called  $K$ -points are not equal to each other because of their orientation to the next neighbors and have to be treated independently in the band structure calculation.

### 1.3 Tight-binding model for graphene

The tight-binding model is a powerful tool for calculations of the band structure for atoms with strongly localized electrons. The strong  $\pi$ -bond of the carbon atoms in graphene satisfies this condition. First calculations were already done by Wallace [14] in 1946 to study coupling between single sheets in graphite. Introductions to the tight-binding model can be found in any solid-state textbook and particularly for graphene in [15]. For our discussion we only take into account nearest neighbors. For a more precise calculation see [16]. We can use the chemical equivalence between A and B atoms in the lattice and write down the secular equation [15] for graphene as:

$$\begin{vmatrix} H_{AA} - ES_{AA} & H_{AB} - ES_{AB} \\ H_{AB} - ES_{AB} & H_{AA} - ES_{AA} \end{vmatrix} = 0 \quad (1.5)$$

The Hamiltonian  $H_{ij}$  and overlap matrix elements  $S_{ij}$  are given by:

$$H_{AA} = H_{BB} = \frac{1}{N} \sum_{R,R'} e^{ik(R-R')} \langle \phi_A(r-R') | H | \phi_A(r-R) \rangle = \epsilon_{2p} \quad (1.6)$$

$$\begin{aligned} H_{AB} &= \frac{1}{N} \sum_{R,R'} e^{ik(R-R')} \langle \phi_A(r-R') | H | \phi_B(r-R) \rangle \\ &= \frac{1}{N} \sum_{R,R'} t e^{ik(R-R')} = \sum_{i=1}^3 t e^{ik\delta_i} \end{aligned} \quad (1.7)$$

where

$$\Phi_j(\vec{k}, \vec{r}) = \frac{1}{\sqrt{N}} \sum_{\vec{R}} e^{i\vec{k}\vec{R}} |\phi_j(\vec{r} - \vec{R})\rangle, \quad (j = 1, \dots, n) \quad (1.8)$$

denotes the Bloch wave function and  $\phi_j$  gives the atomic wave function for an atom at position  $\vec{R}$ . The element  $H_{BA}$  is given by the complex conjugation of  $H_{AB}$  which is real, and thus  $H_{BA} = H_{AB}$ . The largest contribution of  $H_{AA} = \langle \phi_A(r-R) | H | \phi_A(r-R) \rangle$  comes from the term  $R=R'$  and is denoted as the orbital energy  $\epsilon_{2p}$ , whereas the maximum contribution for the transfer integral  $t = \langle \phi_A(r-R+\delta_i) | H | \phi_B(r-R) \rangle$  arises from neighbors. Higher order terms only give a small contribution and are neglected for simplicity. Furthermore we have used the fact that any position vector  $\vec{R}'$  for nearest neighbors can be expressed by

$\vec{R}' = \vec{R} + \vec{\delta}_i$  (see Fig. 1.3). The matrix elements  $S_{AA}$  and  $S_{BB}$  are equal to one for normalized wave functions. The overlap integrals  $S_{AB}$  and  $S_{BA} = S_{AB}^*$  are:

$$\begin{aligned} S_{AB} &= \frac{1}{N} \sum_{R, R'} e^{ik(R-R')} \langle \phi_A(r - R') | \phi_B(r - R) \rangle \\ &= \frac{1}{N} \sum_{R, R'} s e^{ik(R-R')} = \sum_{i=1}^3 s e^{ik\delta_i} \end{aligned} \quad (1.9)$$

Here we define the overlap integral  $s = \langle \phi_A(r - R + \delta_i) | \phi_B(r - R) \rangle$  for two neighboring atoms A and B. We use the nearest neighbor vectors  $\delta_i$  given by equation (1.2) to calculate the sum:

$$f(\vec{k}) = \sum_{i=1}^3 e^{ik\delta_i} = 2e^{ik_x \frac{a}{2}} \cos(k_y \frac{\sqrt{3}a}{2}) + e^{-ik_x a} \quad (1.10)$$

Thus the secular equation 1.5 in the nearest neighbor approximation for graphene transforms to

$$\begin{vmatrix} \epsilon_{2p} - E(\vec{k}) s f(\vec{k}) & t f(\vec{k}) - E(\vec{k}) s f(\vec{k}) \\ t f^*(\vec{k}) - E(\vec{k}) s f^*(\vec{k}) & \epsilon_{2p} - E(\vec{k}) s f^*(\vec{k}) \end{vmatrix} = 0 \quad (1.11)$$

with the solutions

$$E_1(\vec{k}) = \frac{\epsilon_{2p} + t|f(\vec{k})|}{1 + s|f(\vec{k})|}, \quad E_2(\vec{k}) = \frac{\epsilon_{2p} - t|f(\vec{k})|}{1 - s|f(\vec{k})|} \quad (1.12)$$

where  $|f(\vec{k})|$  is given by

$$|f(\vec{k})| = \sqrt{f(\vec{k}) f^*(\vec{k})} = \sqrt{3 + 4 \cos(k_x \frac{3a}{2}) \cos(k_y \frac{\sqrt{3}a}{2}) + 2 \cos(k_y \sqrt{3}a)} \quad (1.13)$$

The band structure is shown in Fig. 1.4]. The upper anti bonding  $\pi^*$ - (conduction-) and lower bonding  $\pi$ -(valence) band are touching at the six corners of the Brouillon zone. The six  $K$  and  $K'$  point are double degenerated at those points.

We can evaluate the function  $f(\vec{k})$  at the high symmetry points for a small momentum  $\vec{p} = (p_x, p_y)$ .

$$f(\vec{k}) \rightarrow f(\vec{K} + \vec{p}) = \frac{3}{2}a(p_x - ip_y) \quad (1.14)$$

$$f(\vec{k}) \rightarrow f(\vec{K}' + \vec{p}) = \frac{3}{2}a(-p_x + ip_y) \quad (1.15)$$



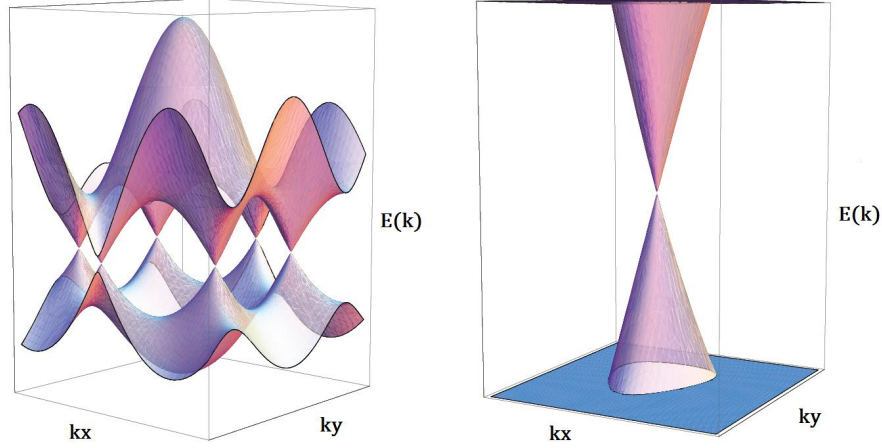


Figure 1.4: Band structure of graphene. Left: The valence and conduction band are touching at the six  $K$  and  $K'$  points that are double degenerated and restrict the honeycomb shaped first BZ. As long as there is no symmetry breaking component in the Hamiltonian, corresponding to i.e. defect, the energy spectrum is gap-less. Right: The zoom-in to one of the high symmetry points shows the linear spectrum for small momenta leading to the description of carriers in graphene as massless Dirac fermion.

Thus we can write the Hamiltonian for low excitation energies at the  $K$  and  $K'$  points as

$$H = v_F \begin{pmatrix} 0 & p_x - ip_y & 0 & 0 \\ p_x + ip_y & 0 & 0 & 0 \\ 0 & 0 & 0 & -p_x + ip_y \\ 0 & 0 & -p_x - ip_y & 0 \end{pmatrix} \quad (1.16)$$

Here we introduced the Fermi velocity  $v_F = \frac{3}{2}at \approx 10^6 \frac{m}{s}$ . The upper left 2x2 block entry describes the Hamiltonian at the  $K$ , the lower right 2x2 entry the Hamiltonian at the  $K'$  point. In the following discussion we only consider  $K$  points but also give the results for the  $K'$  points. The eigenvalues for this Hamiltonian can easily be found by substituting (1.14) into (1.12). The term  $sf(k) \ll 1$  is very small around  $K$  points (small momentum) and can be neglected in the denominator. We set the atomic energy  $\epsilon_{2p} = 0$  and obtain:

$$E_{K,K'}(k) = \pm \frac{3}{2}at|\vec{p}| = \pm v_F p \quad (1.17)$$

where the positive (negative) energy solution belong to electrons in the conduction (valence) band. The linear energy dispersion, which is similar to one for Dirac fermions in Quantum Electro Dynamics, is the most striking feature of graphene. The analogy to relativistic

quantum mechanics becomes even clearer when we express our Hamiltonian in terms of Pauli matrices  $\vec{\sigma} = (\vec{\sigma}_x, \vec{\sigma}_y)$ :

$$H_K = v_F \vec{\sigma} \vec{p} = -i\hbar v_F \vec{\sigma} \nabla \quad (1.18)$$

which indeed is the Hamiltonian for massless fermions [17]. However it is convenient to express the momentum, for example  $p = p_x - ip_y$ , in the complex plane as  $pe^{i\phi_p}$  where  $\phi_p = \arctan(\frac{p_x}{p_y})$  and  $p = p_x^2 + p_y^2$  to solve the eigenvalue equation at the  $K$  point:

$$H\psi(\vec{k}) = E\psi(\vec{k})$$

$$v_F p \begin{pmatrix} 0 & e^{-i\phi_p} \\ e^{i\phi_p} & 0 \end{pmatrix} \psi(\vec{k}) = \pm v_F p \psi(\vec{k}) \quad (1.19)$$

The corresponding momentum space wave functions are given by

$$\psi_{\pm, K}(\vec{k}) = \frac{1}{\sqrt{2}} \begin{pmatrix} e^{-i\phi_p/2} \\ \pm e^{i\phi_p/2} \end{pmatrix}, \quad \psi_{\pm, K'}(\vec{k}) = \frac{1}{\sqrt{2}} \begin{pmatrix} e^{i\phi_p/2} \\ \pm e^{-i\phi_p/2} \end{pmatrix} \quad (1.20)$$

The upper (lower) sign stands for the wavefunction in the  $\pi$ -band ( $\pi^*$ -band) respectively. The fact that graphene's wavefunctions are described by two component spinors amplifies the analogy to massless Dirac fermions. Characteristic for this spinor wavefunction is the sign change upon rotating by an angle  $\phi = 2\pi$  indicating a phase shift of  $\pi$ . It was shown that this so-called Berry's phase in graphene leads to the unusual half-integer Quantum Hall effect [18] (and references there in) and manifests itself in magneto-oscillations [18, 19]. Furthermore the suppression of backscattering processes can be traced to a Berry's phase of  $\pi$  which causes scattering matrix elements [20] to vanish, and explains the high mobility achieved in graphene samples. The Hamiltonian (1.18) is proportional the helicity operator  $\hat{h} = \vec{\sigma} \vec{n}$ , where  $\vec{n}$  is the normalized vector pointing in the direction of momentum  $\vec{p}$ ,  $\vec{n} = \vec{p}/|\vec{p}|$ , and  $\vec{\sigma}$  is the so-called pseudo-spin operator. It is clear from (1.19) that the eigenvalues of  $\hat{h}$  are  $\pm 1$ . The helicity operator gives the projection of the pseudo-spin on the direction of momentum, known as chirality. The pseudo-spin for electrons is parallel to it's momentum at the  $K$  but anti parallel at the  $K'$  points but vice versa for holes (see Fig.1.5). Both pseudo-spin and helicity operator commute with the Hamiltonian which means that pseudo-spin and chirality are conserved close to the  $K$  and  $K'$  points as

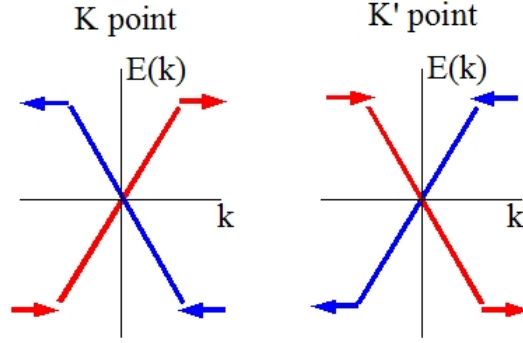


Figure 1.5: The pseudo spin  $\sigma$  is parallel to the momentum for electrons at the  $K$  point but anti-parallel at the  $K'$  and vice versa for holes. The color of the bands indicate that they originate from different sub-lattices.

long as the Hamiltonian is valid. Intervalley backscattering is forbidden due to chirality conservation and backscattering within a cone due to the conservation of pseudospin.

## 1.4 Density of states

Due to its linear dispersion at the K points graphene's density of states (DOS) deviates from that of usual two dimensional electron gas' (2DEG) DOS. The DOS  $\rho(E) = dn/dE$  is the derivative of the number of electronic states per unit area  $n(E)$  with energy smaller than  $E$ . Due to the confinement in two dimension the bands of a 2DEG split into various sub-bands, obeying the parabolic energy dispersion of  $E_F(k) = \frac{\hbar^2 k_F^2}{2m}$ , wherein the density of states is independent of energy.

$$\rho_{2DEG}(E) = \frac{m}{\pi\hbar^2} \sum_{i=1}^n \Theta(E - E_i) \quad (1.21)$$

Here  $\Theta(E - E_i)$  denotes the Heaviside Theta step function and  $n$  gives the number of filled sub-bands. And the Fermi wave vector  $k_F$  is related to the carrier density  $n$  by:  $k_F = \sqrt{2\pi n}$ . We thus have the relation between Fermi energy and carrier density:

$$E_F = \frac{\pi\hbar^2 n}{m} \quad (1.22)$$

For the case of graphene we calculate the DOS per unit area as:

$$\rho(E) = \frac{dn}{dE} = \frac{2g_s g_v \pi k}{\frac{(2\pi)^2}{A_c} A_c} \frac{dk}{dE} = \frac{2}{\pi\hbar^2} \frac{|E|}{v_F^2} \Rightarrow k_F = \sqrt{\pi n} \quad (1.23)$$

where we have used the linear energy dispersion and the spin and valley degeneracy  $g_s = g_v = 2$ . We obtain that the DOS is linear in energy and should vanish at the Dirac point ( $E = 0$ ). The Fermi wave vector is given by  $k_F = \sqrt{\pi n}$ , where the factor of 2 drops out compared to a 2DEG due to the additional valley degeneracy. And since the energy dispersion is linear, the Fermi energy and carrier density are related by:

$$E_F = \hbar v_F \sqrt{\pi n} \quad (1.24)$$

Furthermore it is possible in graphene, since it has no energy gap, to change from electrons to holes as carrier types by adjusting the Fermi level. Naturally, since the valence band is totally filled, the Fermi energy lays at the Dirac point, where the two bands intersect. At this charge neutral point, the conductivity is determined by tunneling effects. However, in experiments one observes a finite conductivity larger than predicted that can be traced back to potential fluctuation caused by the underlying substrate.

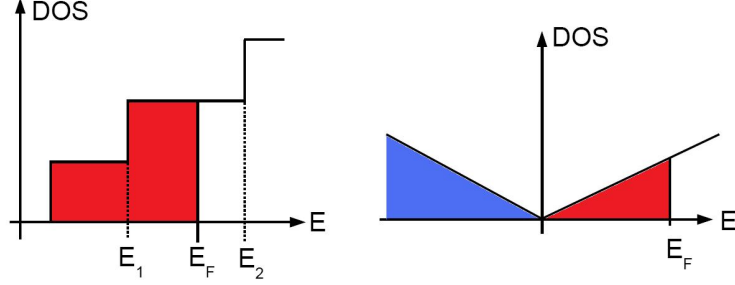


Figure 1.6: Left: DOS of a 2DEG system. Due to the lateral confinement the energy band of the 2DEG splits into various sub-bands. The DOS inside such a band is independent of energy. Right: DOS of graphene. The linear energy dispersion results in a linear DOS that is vanishing at the neutrality point. By shifting the Fermi level through this point the effective charge carriers in the channel can be tuned from holes ( $E_F < 0$ , blue) to electrons ( $E_F > 0$ , red)

### 1.5 Electron hole puddles and scatterers in graphene

The finite conductivity at the Dirac point in non-suspended graphene is mainly due to electron-hole puddles caused by a non uniform potential landscape created by trapped charges in the substrates and chemical doping of graphene. These puddles were observed using a scanning single electron transistor (SET) [21]. They represent omnipresent charge carriers in the graphene and prevent vanishing of the DOS. In the sample studied there, the density fluctuation is of order of  $\Delta n = \pm(10^{10} - 10^{11})\text{cm}^{-2}$ , corresponding to an energy fluctuation  $\Delta E = 10 - 40\text{meV}$ , and is increasing up to a factor of 6 in a magnetic field of  $B = 11\text{T}$  [21]. As we will show later on can extract an estimation for the puddle size from transport data in zero magnetic field. Our samples usually show fluctuation of  $\Delta n \approx 8 * 10^{10}\text{cm}^{-2}$  ( $\Delta E \approx 30\text{meV}$ ), which is comparable to the result of the SET measurement. For graphene on a substrate the unavoidable potential fluctuations indeed constitute the largest part of the disorder in a sample [22]. Further contributions to the disorder are given by ripples, lattice defects and impurities. For an overview of this topic see Ref.[23]. However, the minimum conductivity for graphene was also predicted in many theories (see e.g. [24] and references therein) even without taking into account the effect of electron hole puddles. Earlier theories calculate  $\sigma_{min} = \frac{4e^2}{h\pi}$ , equivalent to  $\rho_{max} \approx 20k\Omega$ , what so far was not experimentally found for graphene on a silicon substrate. Usual obtained values are about three times smaller and are better described by  $\sigma_{min} = \frac{e^2}{4h}$  [25]. The

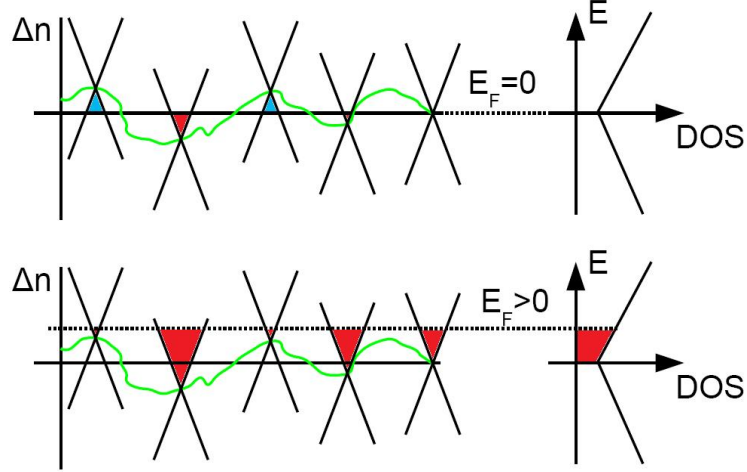


Figure 1.7: Electron hole puddles in graphene. Upper: Trapped charges in the substrate and molecules attached to the surface of graphene cause potential fluctuation along the channel resulting in electron (red) hole (puddles) and a non-zero DOS. The last cone represents the situation for pristine graphene where the DOS would vanish at the Dirac point ( $E_F = 0$ ). Lower: By shifting the Fermi level to higher energies the puddles still remain illustrated by the difference of filling of the cones compared to the last cone. The puddles are always present and lead to an artificially high minimum conductivity close to the Dirac point but also act as scatterers what gives rise to an increase of resistance away from the neutrality point.

minimum conductivity in graphene is surely a topic of its' own but not relevant for this work and we want to refer the interested reader to a more recent work [26], that contains relevant references. As discussed above the quality of the substrate has a main influence on graphene. Not only trapped charges in the silicon oxide layer but mainly impurities on the surface impose limitations on the samples quality. It has been shown in [27] that an increase of the puddle size, for example by treating the substrate with an argon ion bombardment prior the graphene deposition, the mobility of the charge carriers as well as the minimum conductivity at the charge neutrality point are strongly reduced. Very high quality samples on silicon substrate show mobilities up to  $20.000 \text{ cm}^2 \text{ V}^{-1} \text{ s}^{-1}$  and a maximum resistivity  $\rho_{max} \approx 5 \text{ k}\Omega$ . Our samples are in a mobility range of  $4.000 - 8000 \text{ cm}^2 \text{ V}^{-1} \text{ s}^{-1}$  and show  $\rho_{max} = 3 - 4 \text{ k}\Omega$  and can be considered as medium quality samples. To reduce the substrate's influence and study the intrinsic properties of graphene one has to work with suspended samples [9, 10] which can be achieved by etching the silicon oxide layer. Suspended graphene samples show a magnificent improvement in mobility and reduction of electron hole puddles. The quality

of the samples can be further improved by current annealing so that mobilities higher than  $100.000\text{cm}^2\text{V}^{-1}\text{s}^{-1}$  are achieved. The energy fluctuations at the Dirac point are less than  $5\text{meV}$  at helium temperature and are mainly caused by impurities bound to graphene. At the same time suspended graphene shows a large temperature dependence [9] in mobility and minimum conductivity that can be attributed to phonon scattering and thermally activated carriers, whereas these mechanisms play an almost negligible role (compared to puddles) in non-suspended graphene. Potential fluctuations and charged dopants with a Coulomb potential fall into the category of long range scatterers, whereas lattice defects (vacancies), phonons and ripples represent possible short range scatterers in graphene. The main scattering mechanisms usually vary from sample to sample. As mentioned above in suspended graphene long range scatterers can be eliminated giving rise to ultra-high mobilities and a well defined Dirac point with a minimum conductivity close to theoretical prediction. For non-suspended graphene, however, long range scatterers will contribute as well. The influence of various scattering mechanisms on the conductivity, depending of the impurity level, has been pointed out by several theoretical papers (see e.g. [28, 29, 24]). Also the predicted asymmetry for scattering of Dirac fermions off positively and negatively charged impurities [30] was verified [31]. It has been shown that carriers interacting with charged impurities attractively are scattered more than when the interaction is repulsive. Increasing the number of scatterers will lead to a smaller mobility (conductivity) for both, electrons and holes, but will enhance this asymmetry [31]. While a shift of the Dirac point to higher (lower) gate voltages is a direct indication of (unintentional) p-type (n-type) doping as we will discuss later.

## 1.6 Influence of metal contacts

To study the electronic properties of graphene it is necessary to contact the graphene via metal electrodes. Therefore it is essential to understand the physics of metal-graphene interfaces. The difference of work functions for graphene  $W_G$  and the metal  $W_M$  will drive a charge carrier transfer at the interface to equilibriate the Fermi levels. In a simple picture the metal will accept (donate) electrons from (to) graphene when  $\Delta W = W_M - W_G > 0$  ( $\Delta W = W_M - W_G < 0$ ) resulting in p-type (n-type) doping and a negative (positive)

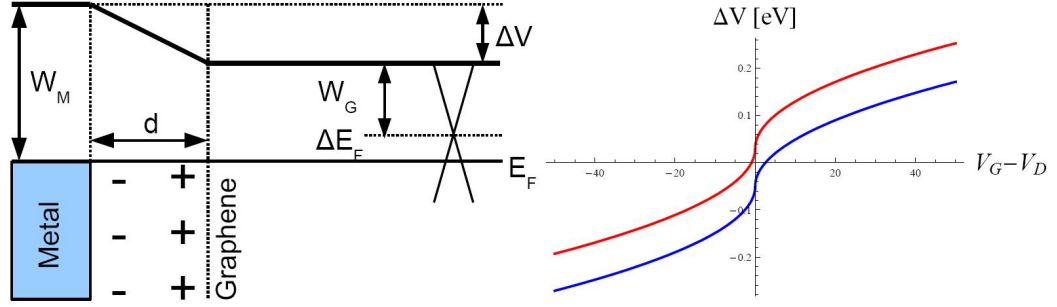


Figure 1.8: Left: Potential step at metal/graphene interface at the charge neutrality point. Here, the metal accepts electrons from graphene, resulting in p-type doping, to compensate the difference in the Fermi level. The spacing between the two materials in equilibrium is calculated to  $d = 3.3\text{\AA}$  [32]. This region is characterized as a dipole layer. The potential step  $\Delta V$  is determined by the difference of work functions and the change of Fermi energy. Right: Dependence of potential step on gate voltage for gold (blue) and titanium (red).

shift  $\Delta E_F$  in the Fermi level. Recent calculation [11] shows however that a mismatch of  $\Delta W > 0.9\text{eV}$  for p-type doping is required, whereas any smaller  $\Delta W$  results in n-type doping. The energy difference of  $0.9\text{eV}$  is contributed to the chemical interaction between graphene and the metal and depends only weakly on the latter. The redistribution of charge at the interface produces a dipole layer that creates a potential step  $\Delta V$  (see. Fig.1.8). This potential step can be expressed in terms of the mismatch of work functions ( $\Delta W$ ) and the Fermi energy shift ( $\Delta E_F$ ) [32]:

$$\Delta V = \Delta W - \Delta E_F + \text{sign}(V_G - V_D) \hbar v_F \sqrt{\pi \alpha |V_G - V_D|} \quad (1.25)$$

Here the  $V_G$  and  $V_D$  stand for the back gate voltage and the position of the Dirac point. The value  $\alpha \approx 7.3 * 10^{10} \text{cm}^{-2} \text{V}^{-1}$  follows from a simple capacitor model that will be explained later. We use titanium/gold contacts with an effective work function (the chemical interaction with graphene is already taking into account) of  $W_{Ti} = 4.3\text{eV}/W_{Au} = 4.7\text{eV}$  for contacting the graphene sheet ( $W_G = 4.5\text{eV}$ ). Since we only use a very thin  $1.5\text{nm}$  layer of titanium it is not guaranteed that it spreads uniformly and the contact to graphene might be formed by gold as well. Since both dope differently, we hope to gain information about the effective doping by a local resistance measurement. The potential barriers at the electrodes could be visualized using photo-current microscopy [32] and from the experimental data the shift in the Fermi level in graphene underneath the contacts was obtained to be  $\Delta E_{F,Au} \approx$



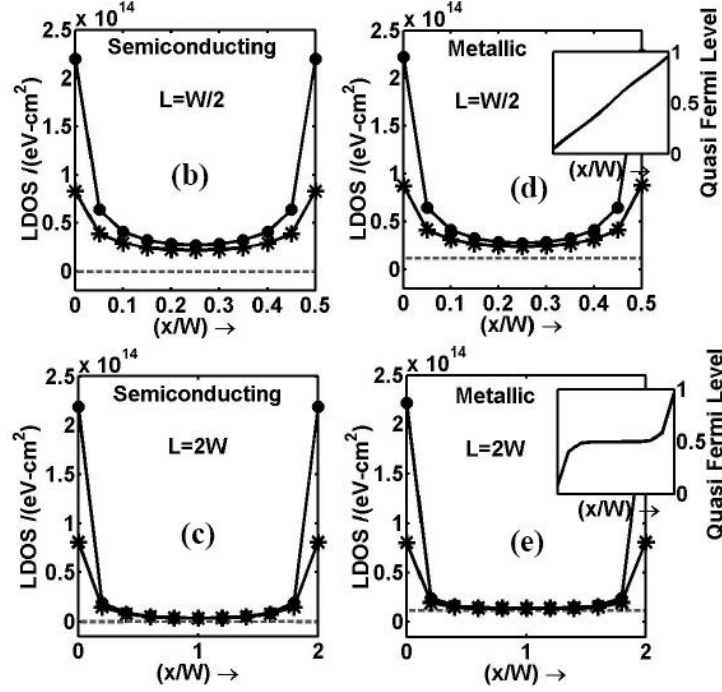


Figure 1.9: Contact induced states in graphene. The graphs represent the result obtained by [33] for a two terminal geometry of different aspect ratio for a metallic and semi-conducting armchair ribbon. For high aspect ratios (see (b) and (d)) the local density of state (LDOS) induced by the electrodes is not vanishing away from the contacts. For smaller aspect ratios (see (c) and (e)) the LDOS will drop sharply to zero in the channel. The inset illustrates the profile of the quasi Fermi level for diffusive (d) and ballistic (e) channel respectively.

$-0.23\text{eV}$  and  $\Delta E_{F,Ti} \approx 0.20\text{eV}$  for gold and titanium. This gives rise to a potential step of  $-50\text{meV}$  ( $+30\text{meV}$ ) at the gold/graphene (titanium/graphene) interface (see Fig.1.8) that will change with back gate voltage. We can calculate the induced carriers  $\Delta n$  by integrating over the linear DOS of graphene (Eq.1.23):

$$\Delta n = \frac{\Delta E_F^2}{\pi v_F^2 \hbar^2} \quad (1.26)$$

that results in n-type (p-type) doping by gold (titanium) with  $4.6 \times 10^{12}$  electrons  $\text{cm}^{-2}$  ( $3.9 \times 10^{12}$  electrons  $\text{cm}^{-2}$ ) underneath the electrodes. It can be seen in the optical experiment [32] this doping is not confined to the contact area but penetrates sub-micron distances inside the graphene. Calculation show [33] that these contact induced states have an impact on the minimum conductivity in graphene and strongly depend on the geometry of the channel and the contacts (see Fig.1.9). Particularly for wide but narrow samples with a high aspect ratio ( $W > L$ ) this can lead to a punch through (non-vanishing) of the DOS of metal

induced states along the graphene channel. On the other hand for channels with  $L > W$  the metal induced states are non-zero close to the electrodes but dropping sharply. The induced carriers create a local charge inhomogeneity and an artificially high conductivity [27]. The creation of potential steps along the interface results in an excess or decrease, depending on the dopant, in resistance, particularly in two terminal measurements. This is consistent with the observed electron-hole asymmetry in graphene using invasive contacts [34]. To minimize the influence of electrodes it is advisable to use either side external or external probes, since they only very weakly couple to the graphene channel, rather than invasive contacts [34]. But for both cases narrow electrodes with width  $W_{el} \ll W$  much smaller than the channel width  $W$  will exert weakest effect on the graphene [33]. To examine the properties of graphene very close to the current probes it is not possible to operate with external electrodes. Thus we use only 100nm wide invasive voltage probes located about 200nm away from the current leads. Another advantage of using small voltage probe is the possibility of measuring local effects that might be hidden when using wide leads that are averaging over their width.

## 1.7 Magnetotransport

### 1.7.1 Classical Hall Effect

In the simple Drude model that treats electrons in crystal lattice classically the equation of motion is given by:

$$m^* \dot{\vec{v}} = -e\vec{E} - m^* \frac{\vec{v}}{\tau} \quad (1.27)$$

where  $m^*$  is the effective mass of the electron,  $e$  the charge of the electron,  $\vec{v}$  its' velocity and  $\vec{E}$  the electric field. The time between two scattering processes of the electron with heavier ion cores, impurities or defects is called scattering time  $\tau$  and adds an additional damping term in the equation of motion. Without this term the electrons would be accelerated constantly by the electric field and Ohm's law would not hold. In presence of an electric field  $\vec{E}$  and magnetic field  $\vec{B}$  we can write (1.27) as:

$$m^* \dot{\vec{v}} = -e(\vec{E} + \vec{v} \times \vec{B}) - m^* \frac{\vec{v}}{\tau}, \quad (1.28)$$

where the additional term  $e(\vec{v} \times \vec{B})$  describes the Lorentz force on the carrier. In stationary conditions  $\dot{\vec{v}} = 0$ , for an electric field in the xy-plane and a magnetic field in the z-direction (see Fig1.10) we can solve (1.28) and obtain:

$$v_x = -\frac{e\tau}{m^*} \frac{1}{1 + \omega_c^2 \tau^2} (E_x - \omega_c \tau E_y) \quad (1.29)$$

$$v_y = -\frac{e\tau}{m^*} \frac{1}{1 + \omega_c^2 \tau^2} (\omega_c \tau E_x + E_y) \quad (1.30)$$

Here we introduce the cyclotron frequency  $\omega_c = \frac{eB}{m^*}$ . The magneto-conductivity tensor  $\vec{\sigma}(B)$  relates the current density  $\vec{J} = ne\vec{v}$  with the electric field:

$$\vec{J} = \vec{\sigma} \vec{E} \quad (1.31)$$

and therefore the magneto-conductivity tensor is given by:

$$\vec{\sigma}(B) = \frac{ne^2\tau}{m^*} \frac{1}{1 + \omega_c^2 \tau^2} \begin{pmatrix} 1 & -\omega_c \tau \\ \omega_c \tau & 1 \end{pmatrix} = \frac{\mu ne}{1 + \mu^2 B^2} \begin{pmatrix} 1 & -\mu B \\ \mu B & 1 \end{pmatrix}, \quad (1.32)$$

where we have used that the ratio of scattering time  $\tau$  to the effective mass  $m^*$  can be expressed in terms of the mobility  $\mu$  of the carrier. However, in experiment it is not possible

to determine the conductivity of a sample directly but rather its' resistance by measuring the voltage drop for a given current. The resistivity of the sample is then simply obtained by dividing the resistances by the the corresponding aspect ratio  $L/W$ , where  $L$  is the distance between the voltage leads and  $W$  the width of the sample. The magneto-resistivity tensor  $\vec{\rho}(B)$  is the inverse of the conductivity tensor  $\vec{\sigma}(B)$ :

$$\vec{\rho}(B) = \vec{\sigma}^{-1}(B) = \frac{1}{ne\mu} \begin{pmatrix} 1 & \mu B \\ -\mu B & 1 \end{pmatrix} \quad (1.33)$$

Thus, in this simple model we obtain that the longitudinal resistance  $\rho_{xx} = \frac{1}{ne\mu}$  is independent of the applied magnetic field. Furthermore the Hall resistance  $\rho_{xy} = -\frac{B}{ne}$  determines the charge carrier density and the sign of the carrier (electrons or holes) and is independent from the scattering time and effective mass. We use the relation (1.33) to transform equation (1.31) to:

$$\begin{pmatrix} E_x \\ E_y \end{pmatrix} = \vec{E} = \vec{\rho} \vec{J} = \begin{pmatrix} \rho_{xx} & -\rho_{yx} \\ \rho_{yx} & \rho_{yy} \end{pmatrix} \begin{pmatrix} J_x \\ J_y \end{pmatrix} \quad (1.34)$$

where we have used that  $\rho_{xy} = -\rho_{yx}$  and  $\rho_{yy} = \rho_{xx}$  as discussed above. In stationary condition when the current density is only along the x-axis ( $J_y = 0$ ) the longitudinal and transverse resistivity are given by:

$$\rho_{xx} = \frac{E_x}{J_x} = \frac{W}{L} \frac{V_x}{I} = \frac{W}{L} R_{xx} \quad (1.35)$$

$$\rho_{yx} = \frac{E_y}{J_x} = \frac{V_y}{I} = R_{xy} \quad (1.36)$$

We see that the transverse resistivity will be independent from the sample geometry and is equivalent to the resistance, whereas the longitudinal resistivity depends of the sample's aspect ratio. Since one can only measure the resistances of a sample and determine it's resistivity, the corresponding conductivities are obtained by inverting the resistivity tensor:

$$\sigma_{xx} = \frac{\rho_{xx}}{\rho_{xx}^2 + \rho_{xy}^2} \quad (1.37)$$

$$\sigma_{xy} = \frac{\rho_{xy}}{\rho_{xx}^2 + \rho_{xy}^2} \quad (1.38)$$

The occurrence of the transverse electric field  $E_y$  is called Hall effect. It exists due to accumulated charges at the borders of the sample that are deflected by the magnetic field.

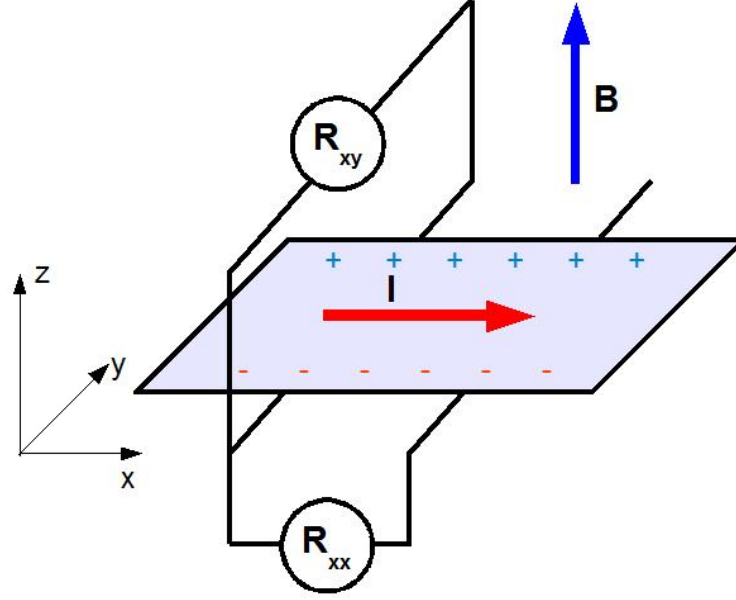


Figure 1.10: Classical Hall effect. For an electric field in x-direction holes and electrons in a conductor are moving in opposite directions but are deflected to the same edge by an applied magnetic field due to the Lorentz force. The signs at the edges mark the predominance of one carrier type. The cross-applied electric and magnetic fields lead to the occurrence of an electric field transverse to the current so that a Hall voltage appears.

The Hall effect was first measured by Edwin Hall in 1879 [35]. It allows determining the type of charge carriers and their density in any conductor and to measure magnetic fields (Hall probe/sensor).

This discussion is rather simplified since we were only considering one carrier type (one band). Many semi-conducting systems for example are better described by a two band model, since electrons as well as holes can contribute to the conduction. Yet both carrier types can have a different mobilities. As long as we assume an electron-hole symmetry in graphene we can assign them the same mobility but either way we will only have one type of carriers since the bands do not overlap. However, if the graphene gets doped, the carriers in the impurity band will have a different mobility and this has to be treated in more sophisticated multi-band model.

### 1.7.2 Multi-band model

In a multi-band model the total conductivity is given by the sum over all contributing bands. Thus we can write the magneto conductivity tensor as:

$$\vec{\sigma}(B) = \begin{pmatrix} \sum_1^n \frac{n_i e \mu_i}{1 + \mu_i^2 B^2} & \sum_1^n \frac{-n_i e \mu_i^2 B}{1 + \mu_i^2 B^2} \\ \sum_1^n \frac{n_i e \mu_i^2 B}{1 + \mu_i^2 B^2} & \sum_1^n \frac{n_i e \mu_i}{1 + \mu_i^2 B^2} \end{pmatrix} \quad (1.39)$$

For a first discussion we take three types of carriers ( $n=3$ ) that contribute to the conductivity of our sample. The intrinsic carriers ( $i=1,2$ ), depending on the back gate voltage, are electrons or holes in graphene, and the extrinsic carriers ( $i=3$ ) are electrons sitting in the impurity band of a p-type dopant. We denote the electron and hole concentration of graphene with  $n_1 = n$  and  $n_2 = p$ , where we have to take into account the charge of the carrier, and the extrinsic concentration of the dopant with  $c$ . Furthermore we assume that electrons and holes will have the same mobility  $\mu_1 = \mu_2$  as discussed above. To simplify presentation of the theory, we will use dimensionless magnetic field  $B * \mu_1$  and inverse mobility of impurity band carriers  $f = \frac{m\mu_1}{\mu_3}$ . Due to the gapless energy spectrum of graphene we can either induce electrons ( $V_G > V_D$ ) or holes ( $V_G < V_D$ ) in our graphene device by sweeping the back gate voltage  $V_G$  through the Dirac point  $V_D$ . The number of carriers induced by gating is  $\alpha(V_G - V_D)$ , where  $\alpha$  is calculated from a simple plane capacitor model. The graphene is separated from the silicon back gate by an insulating  $d \approx 300nm$  thick  $SiO_2$  layer and therefore the induced charge carrier density  $n^*$  is roughly given by:

$$n^* = \frac{Q}{eA} = V \frac{\epsilon_0 \epsilon}{ed} \Rightarrow \alpha = \frac{\epsilon_0 \epsilon}{ed} \approx 7.3 - 8.3 * 10^{10} cm^{-2} V^{-1} \quad (1.40)$$

where  $Q$  is the total charge,  $\epsilon \approx 4 - 4.5$  is the dielectric constant for silicon dioxide and  $\epsilon_0 \approx 8.85 * 10^{12} \frac{F}{m^2}$  the vacuum permittivity. As we will see later  $\alpha$  can deviate significantly from the commonly used value  $\alpha = 7.3 * 10^{10} cm^{-2}$ . The density of electrons is then given by  $n = \alpha V_G - c + \frac{1}{2} \alpha Z$  and for holes by  $p = \alpha V_G + c + \frac{1}{2} \alpha Z$ . The electron-hole puddle size  $Z$ , introduced in an earlier section, is expressed in terms of Volts and assumed to contain electrons and holes in equal measure. Using all that we can calculate  $\rho_{xx}$  and  $\rho_{xy}$

by summing the conductivity tensor 1.39 of the three bands and then inverting to get the resistivity tensor  $\vec{\sigma}(B)$ :

$$\rho_{xx} = \frac{B \left( \frac{cf^2}{F} + \frac{Z\alpha}{1+B^2} + \frac{|c-\alpha V_g|}{1+B^2} \right)}{e \left[ \left( \frac{cf^2}{F} + \frac{Z\alpha}{1+B^2} + \frac{|c-\alpha V_g|}{1+B^2} \right)^2 + \left( \frac{cf^2 B(1+B^2) + (B+f^2 B^3)|c-V\alpha|}{(1+B^2)F} \right)^2 \right]} \quad (1.41)$$

$$\rho_{xy} = \frac{B \left( \frac{cf^2}{F} + \frac{c-\alpha V_g}{1+B^2} \right)}{e \left[ \left( \frac{cf^2}{F} + \frac{Z\alpha}{1+B^2} + \frac{|c-\alpha V_g|}{1+B^2} \right)^2 + \left( \frac{cf^2 B(1+B^2) + (B+f^2 B^3)|c-V\alpha|}{(1+B^2)F} \right)^2 \right]}, \quad (1.42)$$

where  $F = 1 + f^2 B^2 \approx 1$  for fields  $B \leq 3T$  and low mobilities  $f \leq 0.1$  of the extrinsic compared to the intrinsic carriers, which is the typical case for our data. Note, that unlike the case of the single band, the longitudinal resistance now depends on the magnetic field (increasing in field) due to the mixing of resistivity tensors corresponding to different bands. We now can simulate (see Fig.1.11-1.13) the Hall resistance with Eq.(1.44) and examine the influence of the different parameters. Increasing hole-doping is shifting the Dirac point to positive gate voltages, whereas electron-doping shifts the Dirac point to negative voltages. The Hall resistance is decreasing for higher carrier concentrations, as it is already expected in the simple one band model. From Eq.1.44 follows, that for reasonable values of the parameters  $c, f, Z, \rho_{xy}$  will still scale linear with magnetic field for high gate voltages and only close to the Dirac point small deviations will appear. Finally the effect of potential fluctuations is to smear out the Dirac point and contribute permanent additional carriers causing a drop in the Hall resistance and a broadening in electron-hole transition area.

It is worth mentioning that the Dirac point, defined as charge neutrality point, and the point where the Hall resistance vanishes  $\rho_{xy} = 0$  will not longer coincide. If the carrier mobilities for the two bands are different, the total charge accumulated at the edge will not be zero, even though the system is neutral in charge ( $c - \alpha V_G = 0$ ), and therefore a finite resistance ( $\rho_{xy}$ ) will be measured. However, as mentioned above, the mobilities are typically so small ( $f \leq 0.1$ ) that this shift ( $\Delta V < 0.1V$ ) is almost negligible and we will refer to the voltage where  $\rho_{xy} = 0$  as Dirac point in our discussion.

So far we have assumed that the doping concentration over the entire energy range will be constant. Yet this will only be the case as long as the acceptor level of the dopant is laying so deep that we cannot deplete the band. We want to introduce a second p-type dopant

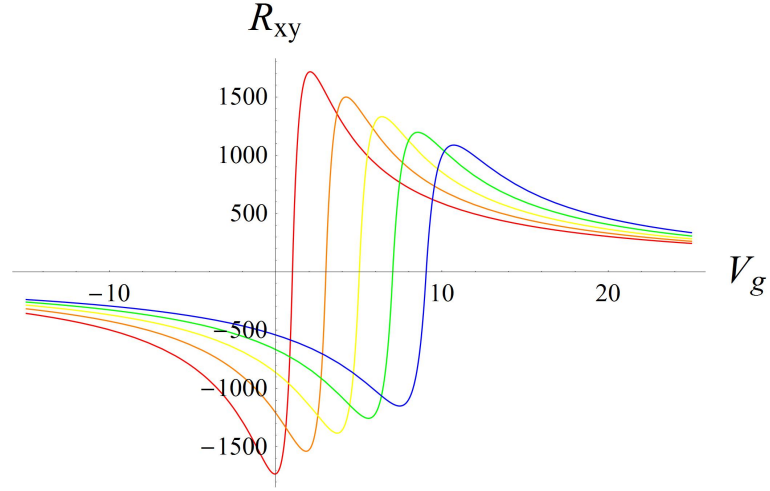


Figure 1.11: Influence of p-type doping on Hall resistance ( $B=1T$ ). Hole doping shifts the Dirac point to positive gate voltages. The shifts depends on the doping concentration  $c$  and increases with cumulative doping. The curves, from red to blue, represent a doping concentration of  $c = 10^{15} - 10^{16} cm^{-2}$ . As already expected in the one band model the resistance decreases with increasing amount of charge carriers.

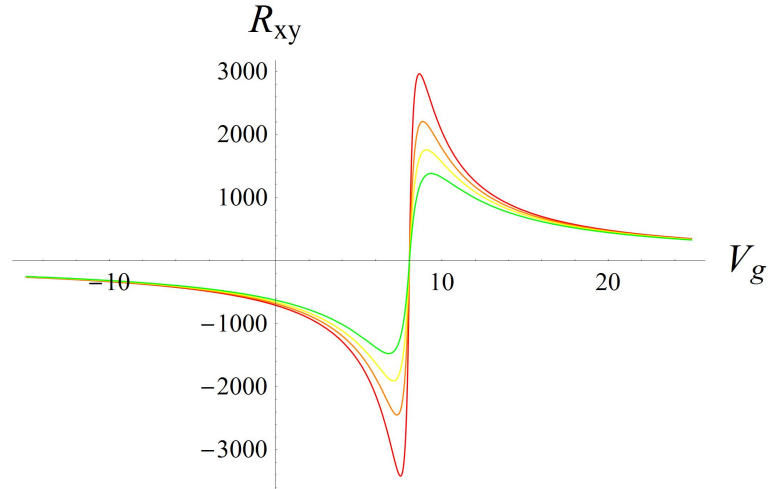


Figure 1.12: Influence of electron hole puddles on Hall Resistance ( $B=1T$ ). The simulation shows that for increasing potential fluctuations  $Z$  the Hall resistance dramatically drops and the transition region from holes to electrons broadens. The red, orange, yellow, green curves correspond to  $Z = 0, 0.3, 0.6, 1V$ .



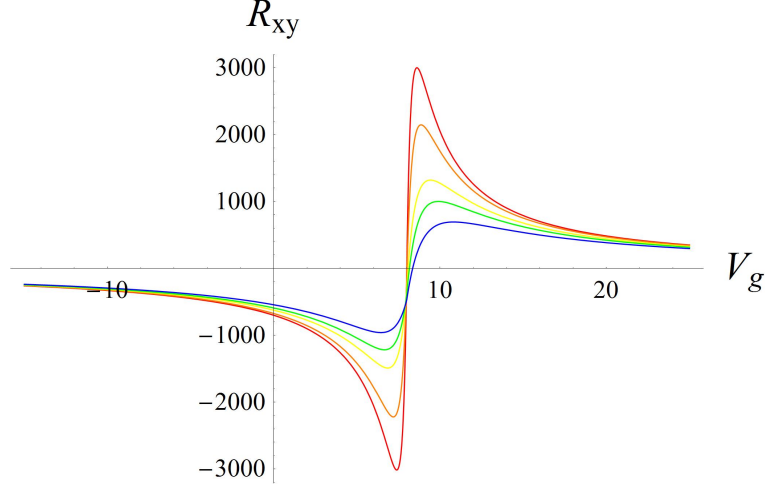


Figure 1.13: Influence of the mobility of the charge carriers in the impurity state on Hall resistance ( $B=1\text{T}$ ). With increasing mobility  $f$  the Hall resistance strongly drops. In addition the slope of the transition area around the Dirac point, where electrons and holes exist at the same time, decreases. A slight shift of the Dirac point due to the mobilities can also be observed. The mobilities are set to  $f = 0.01, 0.03, 0.07, 0.1, 0.15$  for the red, orange, yellow, green and blue curve.

whose energy band sits close to the Dirac point (at small negative energies) and hence can be filled and depleted by shifting the Fermi energy  $E_F$  (sweeping the back gate voltage  $V_g$ ) through it. We can add this dopant to 1.39 which will further extend 1.41 and 1.42 to:

$$\rho_{xy} = \frac{B \left( \frac{cf^2}{F} + \frac{dg^2}{G} + \frac{Z\alpha + |d+c-\alpha V_g|}{1+B^2} \right)}{e \left[ \left( \frac{cf^2}{F} + \frac{dg^2}{G} + \frac{Z\alpha + |d+c-\alpha V_g|}{1+B^2} \right)^2 + \left( \frac{(B+B^3)(dg^2F + cf^2G) + (B+g^2B^3)(B+f^2B^3)|c-V\alpha|}{(1+B^2)FG} \right)^2 \right]} \quad (1.43)$$

$$\rho_{xy} = \frac{B \left( \frac{cf^2}{F} + \frac{dg^2}{G} + \frac{d+c-\alpha V_g}{1+B^2} \right)}{e \left[ \left( \frac{cf^2}{F} + \frac{dg^2}{G} + \frac{Z\alpha + |d+c-\alpha V_g|}{1+B^2} \right)^2 + \left( \frac{(B+B^3)(dg^2F + cf^2G) + (B+g^2B^3)(B+f^2B^3)|c-V\alpha|}{(1+B^2)FG} \right)^2 \right]} \quad (1.44)$$

Here  $d$  stands for the charge carrier density of the dopant and  $g$  for its' mobility.  $G = 1 + g^2B^2$  is defined similar to  $F$  and can be set to  $G \approx 1$ . Again, for electron doping we simply have to change the sign of  $d$ . The total doping concentration is thus given by  $c + d$ . We follow Ref.[36] and assume that the density of states of the two dopants are peaked around two distinct energies  $E_c, E_d$  and replace  $c$  and  $d$  with:

$$c \rightarrow c \int_{E_0}^{E_F} \delta_c(E - E_c) dE \quad , \quad d \rightarrow d \int_{E_0}^{E_F} \delta_d(E - E_d) dE, \quad (1.45)$$

where the  $\delta$  peaks are taken as a Gaussian distribution over a small energy range, corresponding to a voltage range of about 2V. The energy  $E_0$  is the lower bound for the

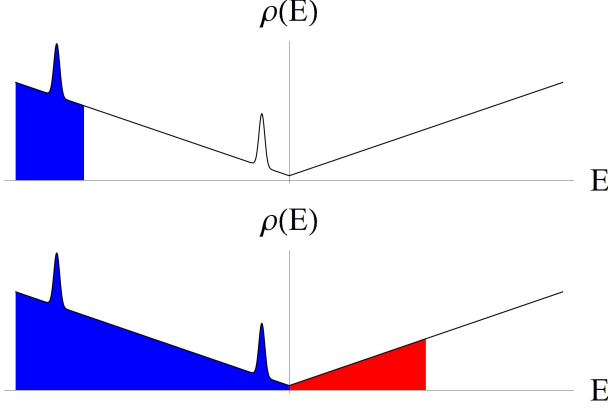


Figure 1.14: Density of states for hole doped graphene. The DOS of the dopants are peaked around two distinct energies and is added to the linear DOS of pristine graphene. The red colored area shows the electron-filled states when  $E_F \geq 0$ . The number of holes is equal to the uncolored area when  $E_F \leq 0$ . Depending on the Fermi level the impurity bands can either be filled or depleted.

integration and can be chosen arbitrarily with the constriction that it has to be smaller than  $E_c$  and  $E_d$ . Fig.1.14 shows the density of states for hole doped graphene taking also into account electron hole puddles. The second dopant will cause a further shift of the Dirac point and when it is sitting close to it, it will lead to a wide broadening of the curve around the charge neutrality point, as it is shown in Fig.1.15, since it can be filled and depleted.

Unfortunately our samples get unintentionally doped during the preparation process and it can not be ruled out, that more than just two kind of impurities lead to the disorder, but we find that merely two dopants are needed to get satisfactory results.

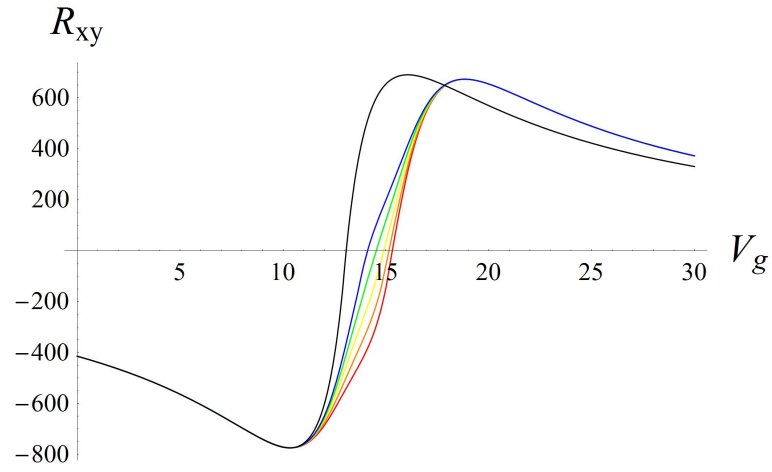


Figure 1.15: Influence of a second p-type dopant on the Hall resistance ( $B=1\text{T}$ ). The dopant sits at low negative energies causing a further shift of  $V_D$  to more positive gate voltages. More important, it has a strong effect (broadening) on the region close to  $V_G$ . The black curve represents the graphene doped with only one p-type dopant with a deep laying band. The colored curves show the effect of a second dopant with a smaller concentration  $c \approx d/2$  situated only  $1 - 2V$  away from  $V_D$

## 1.8 Quantum Hall effect in graphene

More than 100 years after the observation of the classical Hall effect, von Klitzing (1980) and co-workers [7] found a quantized behavior of the transverse resistance in a high mobility silicon MOSFET in a magnetic field of 20T, known as Quantum Hall Effect (QHE). The quantization appears in steps of  $\frac{h}{ie^2}$ , where  $i$  is an integer,  $h$  the Planck constant and  $e$  the electron charge. Probably the most important aspect is, that this quantized resistance of  $R_K = 25.812...k\Omega$  ( $R_K$ , von Klitzing constant) is independent of the material, geometry and macroscopic aspects of the sample and therefore can be used as resistance standard. The reason for this quantization is the applied magnetic field on a 2DEG. It only becomes obvious when we treat the particles quantum mechanically and not with the semi-classical equations of motion as discussed above. For a perfect 2DEG (non-interacting, spinless) placed in a perpendicular magnetic field the Hamiltonian is written as [37]:

$$\frac{\left[\vec{p} + \frac{e}{c}\vec{A}\right]^2}{2m}\psi(\vec{r}) = E\psi(\vec{r}) \quad (1.46)$$

where  $m$  is the effective mass,  $\vec{p}$  the particle's momentum, and  $\vec{A}$  the vector potential associated with the magnetic field  $\vec{B}$  ( $\vec{B} = \nabla \times \vec{A}$ ). This Hamiltonian can be reduced to one similar to the harmonic oscillator and gives quantized energy solution:

$$E_{N,S} = \hbar\omega_c\left(N + \frac{1}{2}\right), \quad N = 0, 1, 2, 3, \dots \quad (1.47)$$

where  $\omega_c = \frac{eB}{m}$  is the cyclotron frequency. The quantized energies are known as Landau levels. The spacing between two levels in a 2DEG is  $\hbar\omega_c$  and typically just is in the order of  $1meV \approx 10K$  in a field of 10T. Thus to resolve these levels one needs very high magnetic fields and low temperatures. For graphene, however, this situation changes dramatically. The Dirac Hamiltonian 1.18 in a perpendicular magnetic field is:

$$v_F \left[ \vec{\sigma} \left( \vec{p} + \frac{e}{c}\vec{A} \right) \right] \psi(\vec{r}) = E\psi(\vec{r}) \quad (1.48)$$

This problem can be solved similar to the 2DEG system. The energy spectrum is [38]:

$$E_N = \text{sign}(N)\hbar\omega_c\sqrt{|N|}, \quad N = 0, \pm 1, \pm 2, \pm 3, \dots \quad (1.49)$$

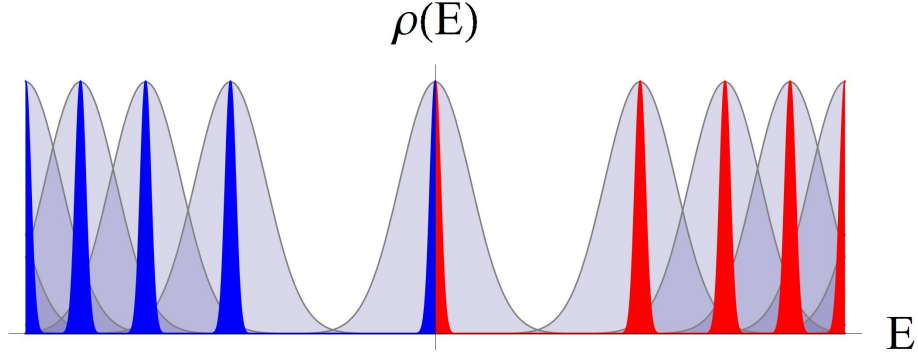


Figure 1.16: DOS of graphene in magnetic field. The linear DOS of graphene is splitting into various Landau levels. The Landau levels are broadened due to disorder into sub-bands. The extended states close to the Landau levels (blue for holes, red for electrons) are current carrying. The localized states (gray shaded) in between two Landau levels can not contribute to the current. The longitudinal conductivity and resistance will vanish at the same time when the Fermi level lies in the region of localized states and Hall resistance plateaus will appear.

The cyclotron frequency  $\omega_c = \sqrt{2} \frac{v_F}{l_B}$  for graphene is given by the ratio of the Fermi velocity  $v_F$  to the magnetic length  $l_B = \sqrt{\frac{\hbar}{eB}}$  that is square root dependent on the magnetic field  $B$ . Substituting this in (1.49):

$$E_N = \text{sig}(N) \sqrt{2e\hbar v_F^2 |N| B} \approx 26 \text{meV} \text{sig}(N) \sqrt{|N| B}, \quad N = 0, \pm 1, \pm 2, \pm 3, \dots \quad (1.50)$$

Graphene's linear DOS splits up into various Landau levels, shown in Fig. 1.16, whose spacings are not any more equidistant in field as for the 2DEG. The spacing for the first to Landau levels is larger than  $100 \text{meV}$  which gives a corresponding temperature of about  $1000 \text{K}$  and lead to the appearance of QHE in graphene even at room temperature [39]. In an ideal system the Landau levels are represented as infinitesimal delta peaks whereas disorder, e.g. impurities, temperature, will broaden those peaks. It was experimentally found, that the width of those Landau sub-bands in a 2DEG is approximately given by [40]:

$$\Gamma = p \sqrt{\frac{B}{\mu}}, \quad p \approx 2.3 \text{meV/T} \quad (1.51)$$

It will broaden with increasing temperature and magnetic field  $B$  and sharpen in high mobility  $\mu$  samples. The degeneracy of a Landau level in a ideal system is the number of

cyclotron orbits that fit in the area of the sample, multiplied by a degeneracy due to spin and valley. The number of states per unit area  $n_B$  is thus given by:

$$n_B = \frac{1}{2\pi l_B^2} = \frac{eB}{h} \quad (1.52)$$

The ratio between the carrier density  $n$  and  $n_B$  is called filling factor  $\nu = \frac{n}{n_B}$  and will be an integer  $i$  for filled Landau levels ( $n = in_B$ ). Substituting this into the Hall resistance  $R_H = \frac{B}{ne}$  leads to the transverse resistance of:

$$R_H = \frac{h}{ie^2} = \frac{R_K}{i} \quad , \quad i = 1, 2, 3... \quad (1.53)$$

when the  $i$ -th Landau level is filled. For an ideal system where the levels are represented as  $\delta$  peaks, separated by an energy gap in the order of  $\hbar\omega_c$ , this can not explain the existence of the resistance plateaus. As long as the Fermi level is located at a totally filled Landau level, where all states are occupied, the longitudinal conductance, and therefore the longitudinal resistance, will vanish, since filled bands can not carry current. But as soon as the Fermi energy rises, electrons will fill the next available free states in the next Landau level. Those states can carry current, the longitudinal conductance and resistance will not be zero any more, and the Hall resistance would simply increase linear with the carrier density. But one has to take into account disorder in the system leading to a broadening of the levels as mentioned above. The density of states is then determined by extended states, close to the Landau level, and localized states in between those levels (see Fig.1.16). Since localized states can not contribute to the current, the longitudinal conductivity and resistivity will still be zero when the Fermi level is shifted through those states. At the same time the number of current carrying extended states is not changing either and the Hall resistance thus shows plateaus. When  $E_F$  is approaching the next Landau level, or better said extended state, electrons can scatter and fill those states. Dissipation will occur, the longitudinal resistance is no longer zero, and  $R_H$  is no longer quantized. As soon as this extended state is filled  $\rho_{xx}$  will drop to zero again and the next plateau in the Hall resistance will show up. This ongoing process can be seen as a transition between localization and de-localization.

We can see from (1.49) that a zero energy Landau level exists at the Dirac point that is shared by electrons and holes. This leads to an additional degeneracy in graphene. The

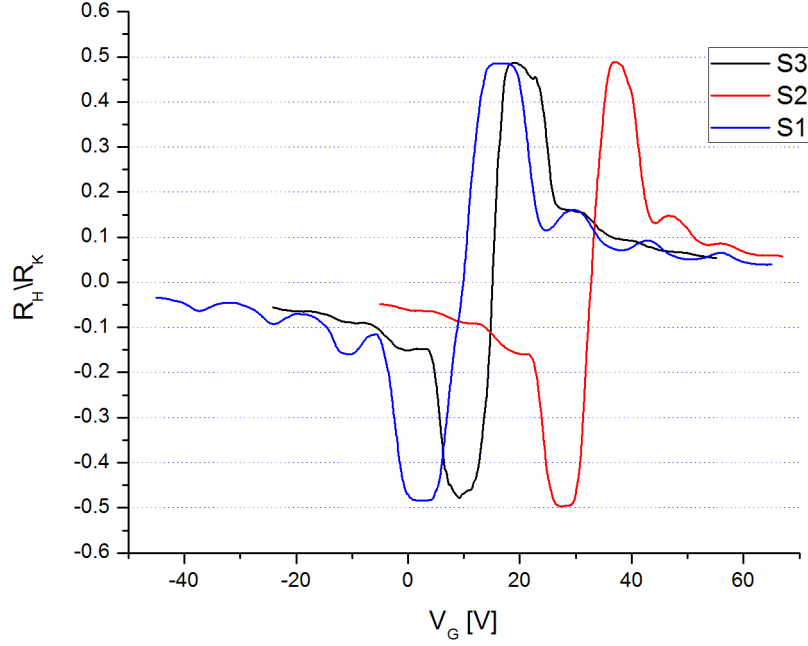


Figure 1.17: QHE in graphene. Our samples show resistance plateaus at values of  $\pm 1/2$ ,  $\pm 1/6$ ,  $\pm 1/10 R_K$  what clearly identifies them as mono-layer. The deviation from the exact values can be explained by the non-vanishing longitudinal resistivity (especially at higher filling factors/electron densities). All measurements were performed at  $T = 4K$  and in fields of  $B = 7T$  for samples S2, S3, and in  $B = 9T$  for S1.

total degeneracy is thus given by  $2(2N+1)$ , where we have taken into account the spin and valley degeneracy  $g_s = g_v = 2$ . The quantized Hall resistance (1.53) is then given by:

$$R_H = \frac{R_K}{2(2N+1)} \Rightarrow \sigma_{xy} = 2(2N+1) \frac{e^2}{h} \quad (1.54)$$

Hall plateaus appear at filling factors of  $\nu = 2, 6, 10, \dots$ . This unusual behavior was first reported by [8] in 2005 and was the first proof that carriers in graphene are described by the relativistic Dirac equation rather than the Schrodinger equation. This quantization is unique for graphene single layers. Graphite devices with two (or more) layers show the plateaus at  $\nu = 4, 8, 12, \dots$  [41]. The unique quantization of single layer graphene can be used to for the clear identification and is shown in Fig.1.17 for our samples.

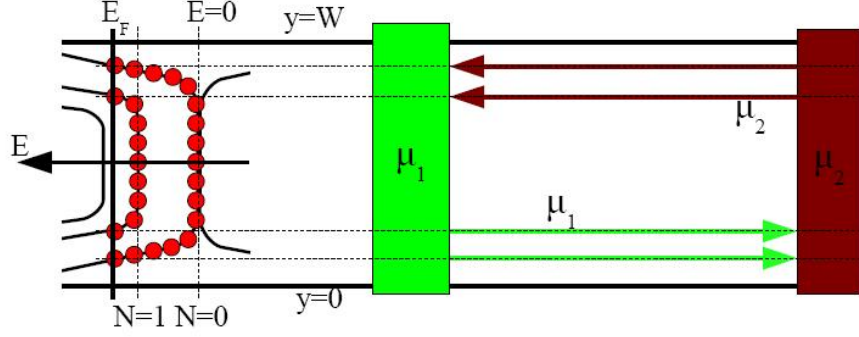


Figure 1.18: Edge states in graphene. The left side represents the energy quantization into Landau levels that bend up due to the confinement of the sample of width  $W$ . All states up to the Fermi level are occupied (red). States of the filled valence band ( $E < 0$ ) are not shown here because it is not contributing to the current. The valley degeneracy of the  $N = 0$  Landau level is lifted at the edge and it splits into two levels, both double spin degenerated, bending to positive and negative energies. The  $N = 0$  level is still fourfold degenerated (spin and valley). This picture corresponds to a filling factor of  $\nu = 2$  with 6 ballistic edge channels at each side with chemical potential of  $\mu_1$  or  $\mu_2$ . The transverse resistance is then given by  $R_H = \frac{R_K}{6}$

## 1.9 Edge states

A common way to describe the transport in the QHE effect is the edge state picture. Every real sample is confined by its edges. The confining potential there results in an upward (downward) bending for positive (negative) Landau levels. Hence, no matter where the Fermi level  $E_F$  is located it will cross extended states at the boundary of the sample, so-called edge states, that can carry the current. In a classical picture those states are described by skipping orbits with the radius of  $l_B$  and the magnetic field will suppress backscattering [42].

Edge states form one dimensional channels each carrying a current of  $I = \frac{e}{h} \Delta\mu$ , where  $\Delta\mu = \mu_2 - \mu_1$  gives the difference of the electro chemical potential of the two current leads. This transport is well described by the Landauer-Büttiker formalism [42, 43] that treats every channel with an corresponding transmission coefficient  $T$  and each contact with a reflection coefficient  $R$ . For ballistic channels and perfect contacts  $R = T = 1$ .  $M$  of those edge channels are thus carrying a current of  $I = M \frac{e}{h} \Delta\mu$ . The carriers in opposite edges are moving in opposite direction due to the band bending and have the chemical potential  $\mu_1$  or  $\mu_2$  of the current lead where they originate from; shown in Fig.1.18. Hence the Hall



resistance is then the ratio of the potential at opposite edges to the current:

$$R_H = \frac{\frac{\Delta\mu}{e}}{M\Delta\mu\frac{e}{h}} = \frac{h}{Me^2} = \frac{R_K}{M} \quad (1.55)$$

For graphene  $M = 2(2N + 1) = 2, 6, 10, \dots$  is given by the number of occupied Landau levels, where  $N = 0, 1, 2, \dots$  is the level index and we obtain the right quantization. Every time the Fermi level is shifted through a higher Landau level an additional channel is added to the system. Since the resistance will be lowest, when the Fermi level lies in between two levels, but highest, when it reaches a new Landau level, one can observe the Schubnikow-de-Haas-effect [\[44\]](#).

## Chapter 2

### Experiment

#### 2.1 Sample Preparation

We deposit highly oriented pyrolytic graphite (HOPG) on a silicon/silicon dioxide (Si/SiO<sub>2</sub>) substrate. The high purity level of HOPG, compared to that of kish or natural graphite, makes it a perfect candidate for transport measurements. The substrate consists of a 740 $\mu$ m layer of Si (p-doped) covered by 300nm SiO<sub>2</sub>. The thickness of the SiO<sub>2</sub> layer is crucial to identify single graphene layers under an optical microscope. The quality of the substrate and the condition and cleanliness of its surface might be decisive for the sample quality. As far as our experience goes graphene deposited on a freshly cleaned substrate shows higher mobilities. Therefore we clean the substrate in a UV ozone cleaner (UVOCS Inc. Model TO 0306) for 15 minutes to remove organic contaminations and bake it afterwards for 30 minutes on a hot plate at 230°C to remove water and organic residues.

We use a pair of tweezers to grab a very thin foil of graphite from the HOPG block and put it on the substrate. We use compressed high purity nitrogen gas applied through an air gun to gently press the graphite foil on the substrate for a few seconds and finally remove it by blowing it away. Now the substrate has to be checked thoroughly under an optical microscope (Nikon Eclipse LV 100) for single layers. We repeat this process until promising flakes are found (see Fig.[2.1]).

To prepare the sample for electron beam lithography we coat it with poly methyl methacrylate resist (MICRO CHEM 950PMMA A 3). Spinn-coating the substrate for one minute at 3000rpm forms a uniform  $\approx$ 100nm thick film of PMMA that polymerizes by baking for 90 seconds at 180°C. It is a positive side effect that graphene is now protected from further contaminations under the coating.

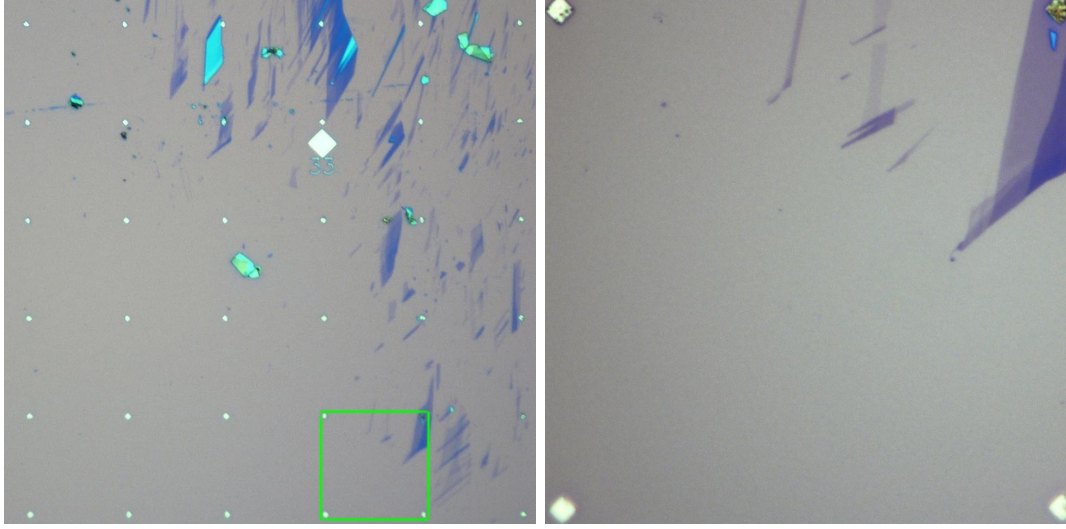


Figure 2.1: The left picture shows a typical graphite field after deposition taken by an optical microscope with 20x magnification. One of the large alignment marks (33 mark) can be seen. The small marks confine region of the size of  $70 \times 70 \mu m^2$ . Most flakes consist of several multi layers (dark blue) and only a few flakes are suitable single layers. The right picture shows a zoom in (100x magnification) on a  $2.5 \times 11 \mu m^2$  graphene flake in the green marked region.

For designing we use the NPGS (Nano Pattern Generation System) and DesignCAD software. The current leads cross the entire sample to create an uniform current flow throughout the graphene and have a width  $W \geq 500 nm$ . The voltage leads are only about 100-150nm wide to reduce the influence on the sample [33]. For a good contact they should extend into the graphene for at least 500nm but the Hall voltage leads themselves should be separated by more than 500nm to ensure no mutual doping. A typical design is shown in Fig.[2.4].

The substrate is already covered with a field of big and small alignment marks (see Fig.[2.1]). The big marks form  $420 \times 420 \mu m^2$  grids which are subdivided by the small alignment marks to thirtysix  $70 \times 70 \mu m^2$  fields. The shape of the small alignment marks is varied in order to enable the experimentalist to uniquely identify location on the substrate by the shape of the adjacent marks.

## 2.2 Electron Beam Lithography

Electron beam lithography uses the fact that polymer chains can either be cut (positive) or strengthened (negative resist) by electrons. We use positive PMMA resist, thus the

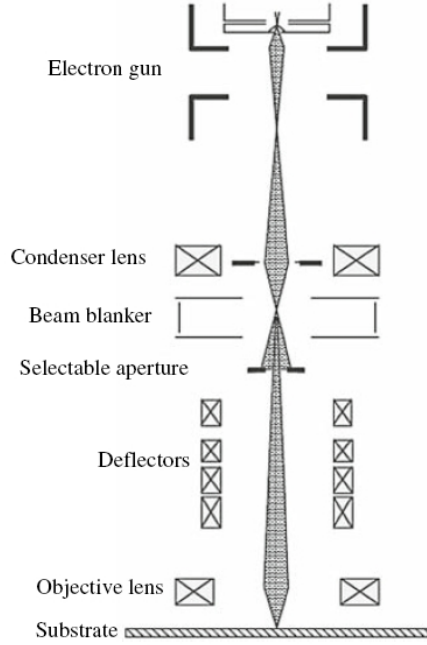


Figure 2.2: The high energy electron beam is controlled and focused by a complex system of lenses and deflectors and irradiates the substrate which is mounted on a mechanical stage (taken from [[46]]). Afterwards the exposed resist can be removed in a developer solution.

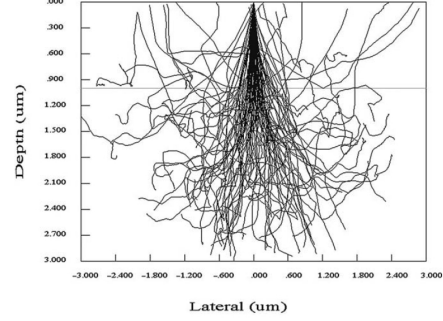


Figure 2.3: Monte Carlo simulation or trajectories for 100 primary electrons with an energy of 50keV. The electrons undergo elastic and inelastic scattering processes in the resist (depth  $\leq 1.0\mu\text{m}$ ) as well as in the substrate. This leads to a broadening in the exposed area (so-called proximity effect) (taken from [[46]]).

polymer-electron interaction breaks chemical bonds of the polymer and forms shorter and lighter molecular chains. The exposed area can be dissolved in a developer solution that removes the low weight polymer fragments but the unexposed resist will not be attacked.[45] The electron beam is generated by an electron gun in a high vacuum ( $2.5 \times 10^{-9} \text{mBar}$ ) and accelerated to 30keV. It is focused by several condenser lenses and controlled by deflectors before it hits the substrate in the main chamber (see Fig.[2.2]) which has a lower vacuum of about  $3 \times 10^{-6} \text{mBar}$ . The substrate is mounted on a high precision mechanical stage. Both beam and stage are computer controlled .

Although the beam can be focused to a spot size smaller than 10nm the writing resolution is limited to  $\approx 20 \text{nm}$ . Unlike optical lithography, where resolution is limited by the wavelength of light, resolution of electron beam lithography is limited due to scattering processes of

Table 2.1: Our design is divided into three sections. All patterns inside the small alignment marks (region 1) are written with a high magnification and low beam current to achieve a high resolution. The large bonding pads in region 3 don't include any fine features and hence a lower magnification can be used. The electrodes connecting these two sections are located in region 2 (see Fig.[2.4]). The order of different doses used in region 1 stands for current lead/close Hall leads/center Hall leads/current lead respectively.

region	magnification	spot size	beam current	dose[unit? C/cm <sup>2</sup> ]
1	800	1	$\approx 15\text{pA}$	380/450/550/450
2	400	3	$\approx 70\text{nA}$	420
3	120	6	$\approx 400\text{nA}$	420

the incoming electrons. High-energy (primary) electrons undergo random inelastic scattering with atoms and elastic scattering with (secondary) electrons which get knocked off the atoms in the resist layer and substrate. Inelastic scattering processes cause chain reactions in random direction involving energy transfer and result in a broadening of the exposed area of the resist(see Fig.[2.3]). Electron scattering is mainly influenced by electron energy, the density of substrate material and the thickness of the resist. In general one can say that for high resolution ( $\ll 100\text{nm}$ ) high beam energies (50-100keV), low substrate densities and thin resist layers are preferred [46]. Our electron beam lithography system (PHILIPS XLFEG/SFEG Scanning Electron Microscope) can operate at a maximum beam energy of 30keV and is limited to a resolution of  $\approx 50\text{nm}$ . As it can be seen in Fig.[2.3] scattered primary electrons can propagate more than one micrometers away from the beam center leading to a weak exposure of neighboring areas. This so-called proximity effect has to be taken into account by reducing the dose (total charge of incident electrons per area) when we write patterns spaced less than 200nm (see Tab.[2.1]).

Our design is written in three different magnifications for three region, regions 1-3 (see Fig.[2.4]), to come to a compromise between writing time and desired resolution. All electrodes inside the small alignment mark field, including the Hall Bar geometry, are written with higher magnification and lower beam current (spot size) for a high resolution. The exact numbers can be found in Tab.[2.1].

After the writing process we develop the sample in a mixture of isopropanol (IPA) and water at a ratio of 3:1 for 120 seconds which is cooled down to 5°C. This developer shows superior lithographic performance in comparison with standard developer (MIBK:IPA)[47]

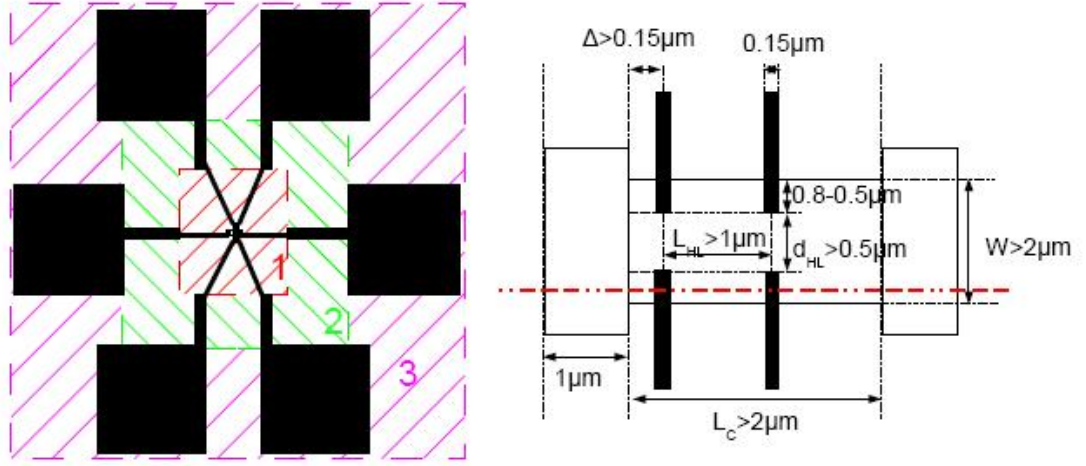


Figure 2.4: The left figure shows a simplified sample geometry. The bonding pads in the purple shaded area (region 3) are  $100 \times 100 \mu\text{m}^2$  large. The bonding pads and the fine structures ( $0.1\text{-}2 \mu\text{m}$ ) of the Hall bar (red shaded/region 1) are connected by  $10 \mu\text{m}$  wide electrodes (green shaded/region 2). The right side shows a detailed view at the Hall bar design. The  $1 \mu\text{m}$  wide current leads are orientated perpendicular to the graphene sheet and run over the entire sample to create an uniform current flow. One pair of Hall voltage leads (width= $0.15 \mu\text{m}$ ) is placed close to one of the current leads (width= $1 \mu\text{m}$ ) in varying distances  $\Delta \geq 0.15 \mu\text{m}$ . The second Hall voltage pair is located in the middle of the sample. The separation  $d_{HL}$  between opposing Hall leads should be greater than  $0.5 \mu\text{m}$ . The two pairs of Hall voltage leads are separated by more than  $1 \mu\text{m}$  ( $L_{HL} \geq 1 \mu\text{m}$ ). To meet all the requirements the graphene should at least have a size of  $2 \times 4 \mu\text{m}^2$ .

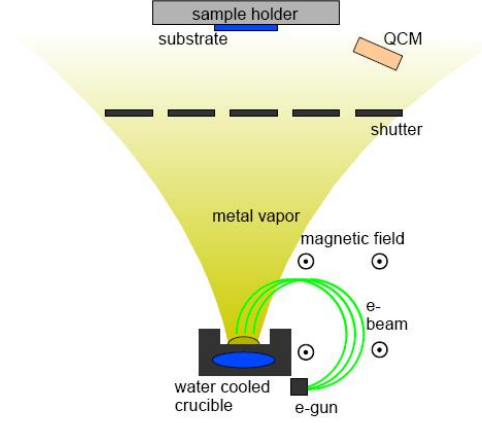


Figure 2.5: A high energetic (4keV) electron beam is bent by a magnetic field towards the the metal target which sits in a watercooled crucible. The metal heats up over its' melting temperature and starts to vaporize. Due to the high vacuum the molecule clusters can propagate ballistic throughout the chamber. They condense on the colder surface of the substrate, chamber wall, and QCM which allows us to control the thickness of the layer. The shutter is needed for a well controlled layer thickness.

and the low temperature further decreases the edge roughness of developed structures [46]. Immediately after development we rinse the sample in IPA for 15 seconds and blow dry it with nitrogen gas. To guarantee good contact between the electrodes and graphene we clean the sample for 70 seconds in the UV ozone cleaner to remove last PMMA residues.

### 2.3 Electron Beam Evaporation

To deposit a thin film of metal in the opening of the polymer resist we use the electron beam evaporation technique (THERMIONICS e-GUN<sup>TM</sup> Model 100-0030). Our sample is placed in a vacuum chamber ( $\leq 5 \cdot 10^{-7}$  mBar) where hot metal vapor condenses on its' cold surface. An electron beam produced by a heated tungsten filament is accelerated to 4keV and is bent by a permanent magnet towards the metal target (see Fig.[2.5]). The targets are sitting in crucibles that are water cooled to prevent it from overheating. When the electron beam hits the target most of its' kinetic energy is transformed to thermal energy. The temperature can be controlled by the beam current that is in the order of 100mA. The metal is heated up to boiling temperature and begins to vaporize. The high vacuum allows the molecules to travel ballistically through out the chamber till they finally condense on

Table 2.2: The deposition rate  $R$  strongly depends on the melting temperature  $T_m$  of the material and therefore on the beam current  $I_b$ . Even though the beam current for aluminum is half of the beam current for titanium the deposition rate is about 5 times higher. Electron beam evaporation allows deposition rates between 1 and 10nm/s [46]. For a given Z-ratio between film material and quartz and density  $\rho_f$  of the film material the thickness of the layer is evaluated according Eq.[2.2] and Eq.[2.3]

material	$T_m$ [°C]	$\rho_f$ [g/cm <sup>3</sup> ]	Z-ratio	$I_b$ [mA]	$R$ [nm/s]	$T_f$ [nm]
titanium	1670	4.5	0.628	100	0.1	2-3
gold	1063	19.3	0.381	80	0.5	28
aluminum	660	2.7	1.08	55	0.5	26

a colder surface (substrate, chamber walls). The deposition rate  $R$  mainly depends on the distance  $r$ , and the difference between the vapor pressure  $P_s(T)$  of the source material, which is a function of temperature  $T$ , and the pressure in the vacuum chamber  $P_c$  [46].

$$R \propto \frac{P_s(T) - P_c}{r^2} \quad (2.1)$$

The film thickness is controlled by a quartz crystal monitor (QCM). The frequency of the quartz crystal is very sensitive to the mass change  $\Delta m$  per surface area  $A$ . The dependence of frequency change  $\Delta f = f_u - f_l$  between the unloaded ( $f_u$ ) and loaded ( $f_l$ ) quartz crystal and  $\Delta m$  is given by the Lu and Lewis equation [48].

$$\frac{\Delta m}{A} = \frac{N_q \rho_q}{\pi Z f_l \tan [Z \tan [\frac{\pi \Delta f}{f_u}]]} \quad 1, \quad Z = \sqrt{\frac{\rho_q \mu_q}{\rho_f \mu_f}} \quad (2.2)$$

Here  $N_q$  is a frequency constant for the quartz crystal,  $\rho_q$  ( $\rho_f$ ) is the density,  $\mu_q$  ( $\mu_f$ ) the shear modulus of the quartz (film material) and  $Z$  is the Z-ratio for the film material. The film thickness  $T_f$  is given by:

$$T_f = \frac{\Delta m}{A \rho_f} \quad (2.3)$$

We use the parameters given in Tab.[2.2] to evaporate a 2-3nm thick film of titanium followed by 28nm (26nm) film of gold (aluminum). The thin titanium layer guarantees a good wetting of gold (aluminum) and improves the contact quality. After the deposition process is completed we insert the metal coated substrate into acetone which dissolves resist. The overlying layer is lifted off and removed and only the desired pattern remains. To avoid acetone residues we immediately rinse the substrate thoroughly in IPA and blow dry it with nitrogen gas. Fig.[2.6] recapitulates the most important steps of the preparation



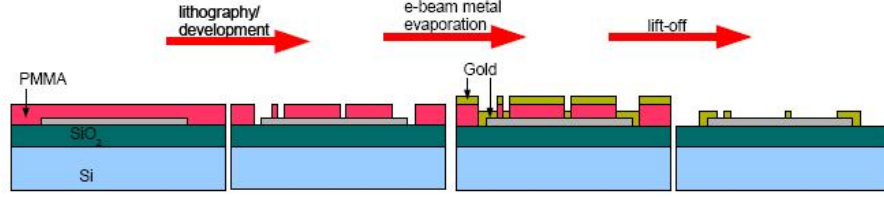


Figure 2.6: Profile of the design marked by the red dashed line in Fig.[2.4]. After the graphene flake is deposited on the Si/SiO<sub>2</sub> substrate and coated with PMMA the resist is exposed to a 30keV electron beam and developed in a water/IPA mixture. A thin film of Ti/Au (Ti/Al) is deposited and the lift-off in acetone removes the overlying layer.

process. An optical image of one structure is shown in Fig.[3.6] in a later section. As prepared, the graphene is exposed to various organic compounds (PMMA, acetone, IPA) which can settle on its' surface. Furthermore the samples get p-doped, likely by water. Hence to clean the sample from dopants and organic residues we anneal the sample at 200°C in forming gas (10%H, 90%Ar) for 2 hours.

## 2.4 Experimental setup

After baking we mount the sample with rubber cement and silver paint on our sample holder (Fig.2.7,b). The silver paint serves as connection to the Si-layer of the substrate that acts as back gate. Before wire bonding the sample with 25 $\mu$ m thin aluminum or gold wires to the connection pads of the sample holder it is advisable to protect the sample by a shunt resistance, also known as crowbar circuit. In our case this is achieved by shorting all pads, except the one used for back gate, by wrapping a high conductive wire around the connection pins (Fig.2.7,a). Any over-voltage will drop at this parallel short because of its' low resistance of a few Ohms rather than at the sample ( $R \approx 1k\Omega$ ). Usual graphene samples are only a few microns wide and easily destroyed by currents higher than 1mA. Any static shock, e.g. by touching one of the pins, is a potential threat and should be avoided. A further preventive measure to minimize risks of damaging the sample by static shocks is to ground oneself anytime one is working with the sample. We use coax cables with pin connectors (Fig.2.7,c) in our insert which are connected to a further shunt box that can be operated when the insert is loaded in the dewar. This shunt box, consisting of high resistive ( $R = 500k\Omega$ ) potentiometer and switches, is essential for a faultless and

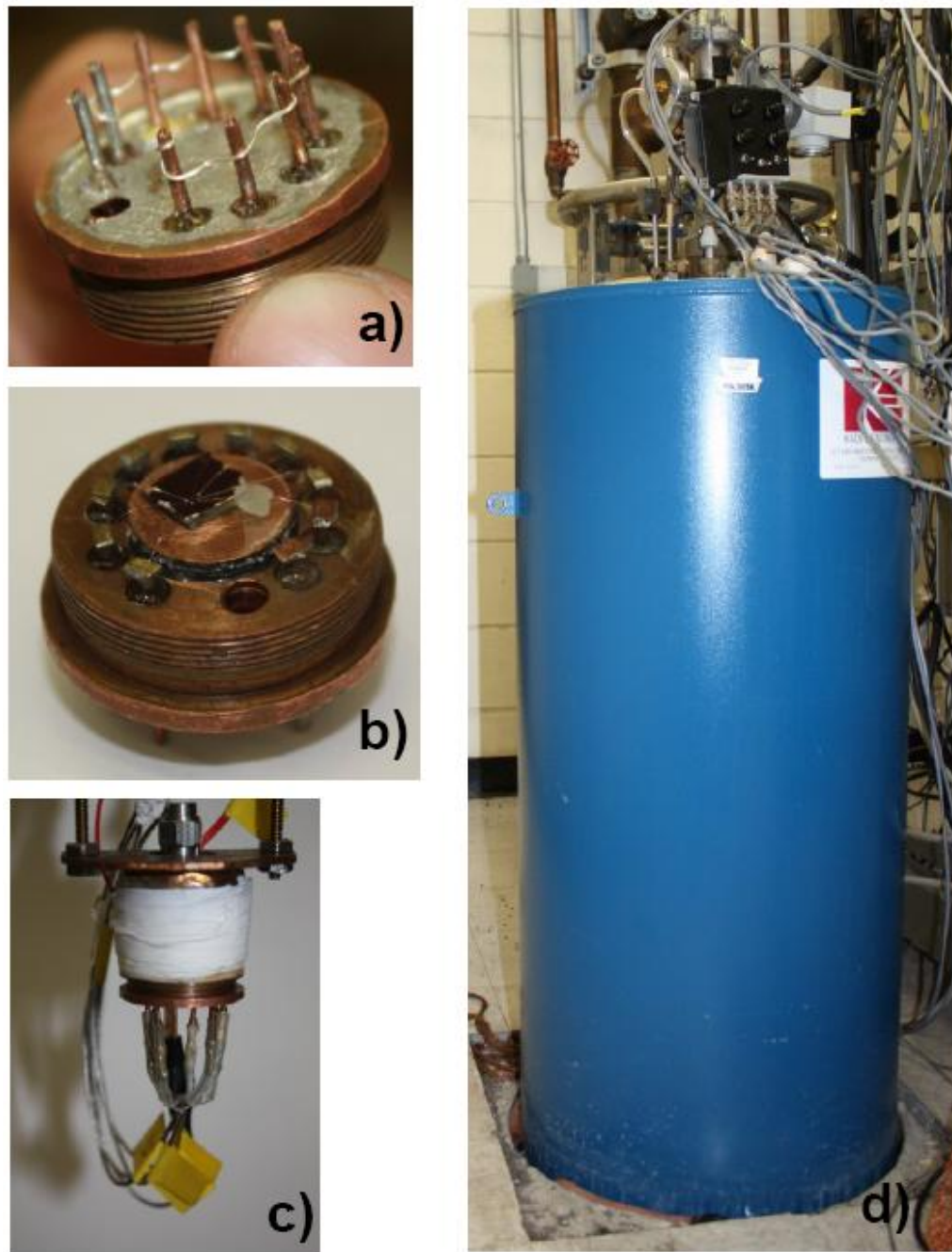


Figure 2.7: a) Bottom view on sample holder. The pins are shorted to protect. Any over-voltage will drop at this very low resistive short-circuit parallel to the sample. b) Sample mounted on holder with rubber cement and silver paint (at the right corner of the substrate). Aluminum wire is used for the wire bonding. c) Sample plugged in the insert. The coax cables with pin-connectors lead to a shunt box on top of the insert. The shunt on the pins has been removed after the connection. d) The insert is loaded into the helium cryostat equipped with a superconducting magnet. The black box on top is our shunt box.

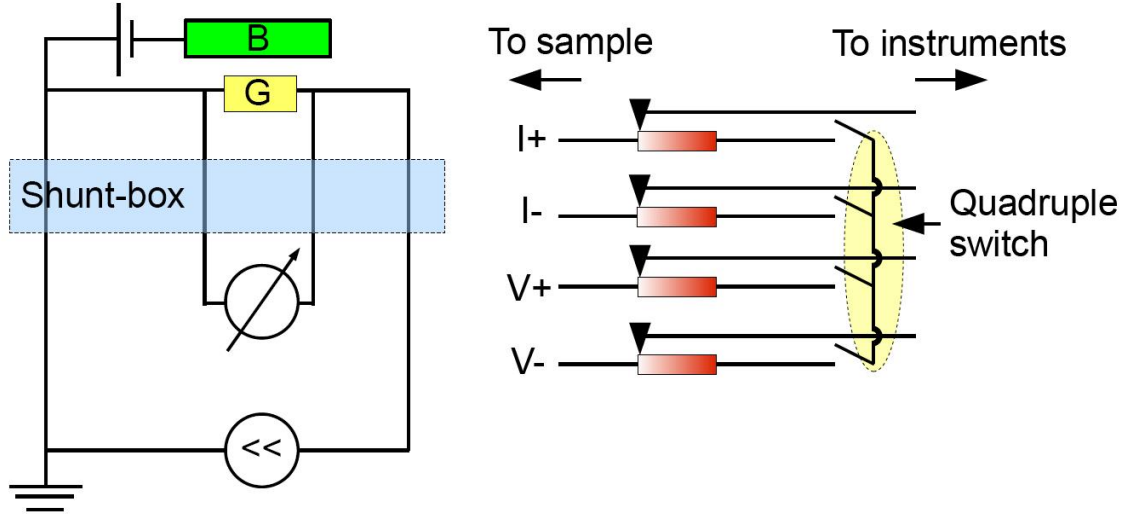


Figure 2.8: Left: Electrical circuit of the measurement. A small current of 100nA with a frequency of 13Hz is passed through the graphene sample  $G$ . The voltage drop across the sample is measured with a Lock-In amplifier. A voltage source is connected to back side of the substrate serving as back gate  $B$ . We use a shunt-box to protect the sample in between measurements (Right). The figure displays the shunt in open position ( $R=0$ , switch open) used for measurements. By flipping the switch and shorting all contacts the sample will be protected. The potentiometer should be in a high resistance position before flipping the switches because discharging of the switches can lead to unintentional high voltages that will drop at the resistors before reaching the sample.

successful measurement (for further explanation see Fig.2.8). During the entire loading process this shunt should be closed to protect the sample after connecting the wires to the samples and removing the shunt from the pins. The insert is closed with a can, sealed with vacuum grease and pumped to a low vacuum. All experiments were done in a helium dewar equipped with a superconducting magnet that can operate in persistent mode (see (Fig.2.7,d). At helium temperature ( $T=4K$ ) a magnetic field up to  $B = 8T$  can be achieved. The experimental setup consists of the following instruments (see Fig.2.9):

- Keithley 6221 DC and AC current source
- Keithley 2400 Sourcemeter
- Keithley 2001 Multimeter
- Stanford Research SR 830 digital Lock-In amplifier
- Princeton Research PR 124A analog Lock-In amplifier

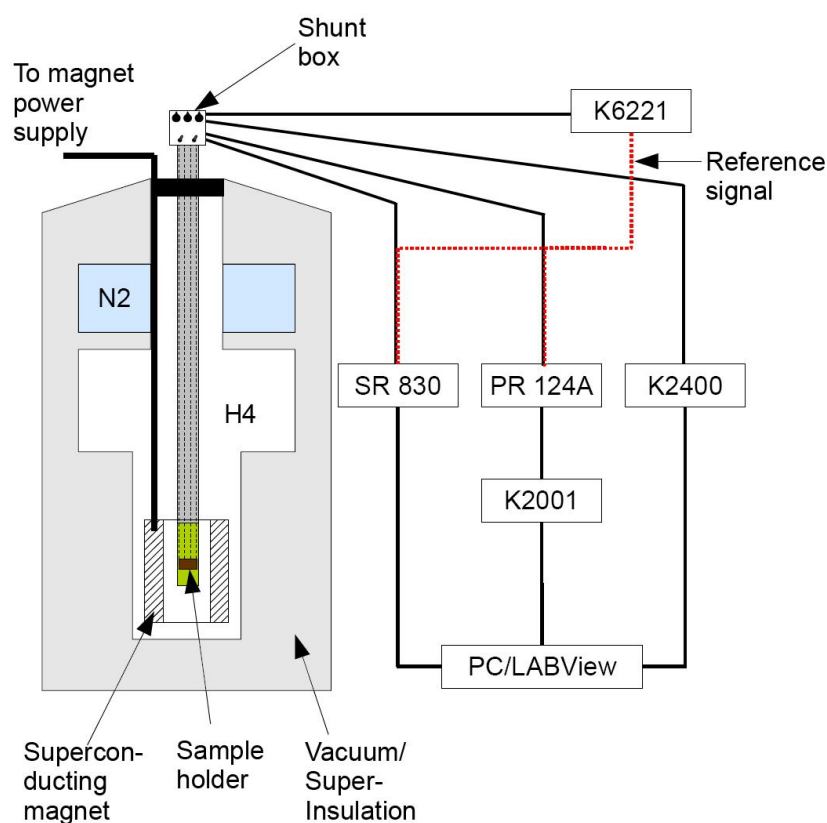


Figure 2.9: Experimental setup. The cryostat is isolated by vacuum, superinsulation that reduces heat dissipation through radiation and some liquid nitrogen N<sub>2</sub>. The superconducting magnet is sitting on the bottom of the cryostat in liquid helium H<sub>4</sub>. The sample holder mounted at the end of the insert is placed in the center of the magnet where the field is homogeneous. The current source is handled manually, the back gate source by a LABView program. The data of the two amplifiers is read by another LABView program and saved on the computer.

To minimize the heating of the sample we use a 100nA AC current produced by the Keithley 6221. The frequency of 13Hz is supplied as reference signal to the Lock-In amplifiers. The use of AC measurements is good for canceling DC offsets. The Lock-In technique further reduces background noises and provides a clear signal. The digital signal of the SR 830 is directly given to the computer whereas the analog signal from the PR 124A first has to be converted to a digital one by the Keithley 2001. The Keithley 2400 is controlling the back gate voltage. All instruments are computer-controlled by LabVIEW programs that are also collecting the data.

## Chapter 3

### Data analysis

#### 3.1 Sample characterization

We will discuss three samples, S1, S2 and S3 with different doping levels and qualities. The samples are designed after Fig.2.4 and the important dimension are summarized in Tab.3.1. The highest quality sample S1 will be of main interest since it has three pairs of voltage leads that let's us compare the results of various spacings  $\Delta$  on one sample. All of the samples are strongly p-type doped resulting in a shift of the Dirac points to positive gate voltages of  $V_{D,S1} \approx 9V$ ,  $V_{D,S2} \approx 31V$  and  $V_{D,S1} \approx 17V$  (see Fig.3.1). The unintentional doping probably occurs during the preparation process. Even though the annealing in forming gas is supposed to remove most of impurities [27], at least at graphene's surface, the exposure to air during the wire bonding might result in heavy doping, depending on exposure time and humidity. The Hall bar geometry allows us to compare the longitudinal resistance along the two edges of the sample. The discrepancy between them can be explained by non-uniform doping, leading to a macroscopic inhomogeneity on the sample. Sample S1 has a well pronounced Dirac peak and shows the lowest doping level, whereas S3 shows a high level of disorder. However, this can not only be traced back to the higher doping level of S3, since S2 with an even higher level of doping shows a better quality. The quality of the sample is usually defined by the carrier mobility, the broadening of the peak, and the

Table 3.1: Dimensions (see Fig.2.4) of samples S1, S2 and S3. Since S1 has three voltage pairs, it has two corresponding  $L_{HL}$ 's and  $\Delta$ 's

Sample	$L_c[\mu m]$	$L_{HL}[\mu m]$	$W[\mu m]$	$\Delta[\mu m]$
1	6	2, 2	2	0.2, 0.4
2	10	3	3	0.15
3	4	1.5	2.2	0.2

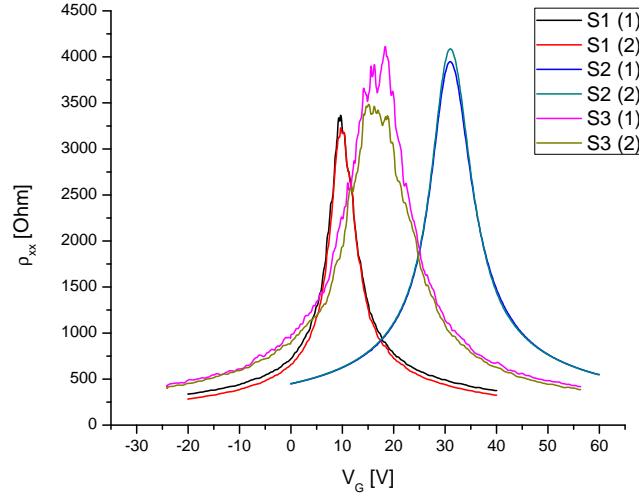


Figure 3.1: Resistivity  $\rho_{xx}$  versus back gate voltage  $V_G$ . All three samples show p-type doping with a shift of the Dirac point to positive gate voltages of 9, 17, and 31V. The numbers in the brackets denote the two edges of the sample.

maximum resistivity. One can shift the Dirac point to zero and plot the resistivity versus the logarithm of the shifted gate voltage, to obtain a rough estimation for the electron-hole puddle size  $Z$ . Since the conduction at the Dirac point can be mainly attributed to the potential fluctuation, the width of the resistance plateaus gives a hint at which gate voltage the electron hole puddles are no longer the dominant carriers. This gives an upper bound for the estimation of  $Z = 0.8 - 2V$  for the samples. The conductivity, equal to the inverse resistivity, shows a linear behavior in S3 suggesting dominant long range scatterers. In contrast S1 and S2 are sub-linear at high carrier concentrations, indicating the existence of short range scatterers [49, 50, 29]. Since  $\sigma \propto (R_{shortrange} + R_{longrange})^{-1}$  and  $R_{longrange} \propto n^{-1}$  one should expect this sub-linearity at high gate voltages, as long as the number of long range scatterers is not too high. This sub-linearity becomes pronounced for high mobility samples (fewer long range scatterers) and thus is another quantity to characterize the sample's quality. The carrier mobility  $\mu$  is derived from the simple Drude model and is shown in Fig.3.4:

$$\rho^{-1} = \sigma = ne\mu \quad \Rightarrow \quad \mu = (ne\rho_{xx})^{-1} = (\alpha(V_G - V_D)e\frac{W}{L}R_{xx})^{-1} \quad (3.1)$$

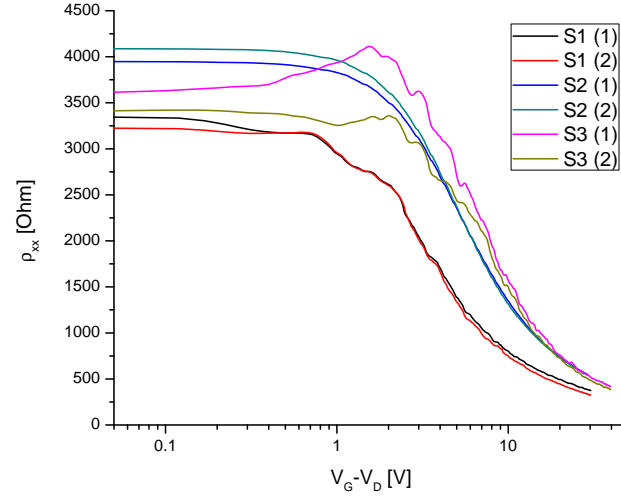


Figure 3.2: Estimation of puddle size  $Z$ . By plotting the resistivity  $\rho_{xx}$  over a logarithmic scale of the shifted back gate voltage  $V_G - V_D$ , we obtain an upper bound for the puddle size  $Z$  of 0.8, 1.2, and 2V for S1, S2, and S3 respectively.

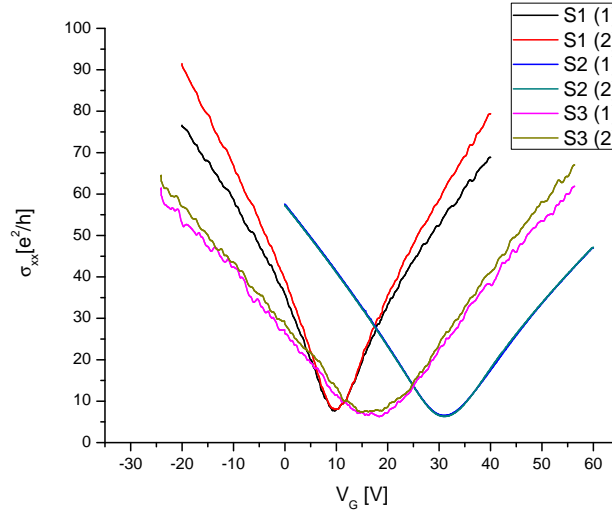


Figure 3.3: Conductivity  $\sigma_{xx}$  versus back voltage  $V_G$ . The sub-linearity of  $\sigma_{xx}$  for S1 and S2 results from the interplay of short and long range scatterers. Sample S3 is dominated by long range scatterers leading to its' linear behavior



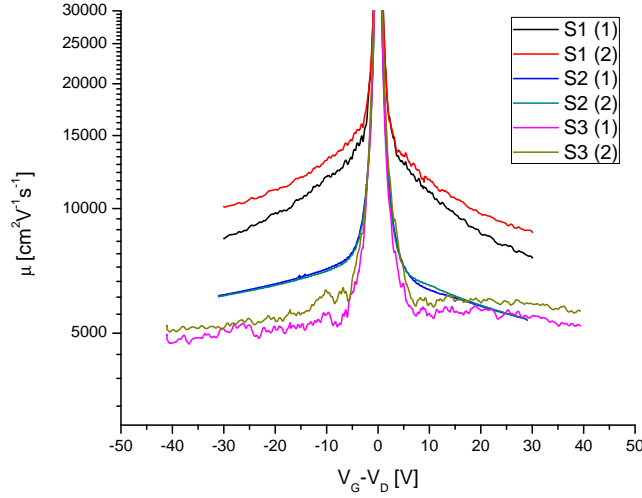


Figure 3.4: Mobility  $\mu$  versus back gate voltage. Because of its' linear dependence of conductivity on the back gate voltage sample S3 leads to a constant mobility  $\mu$  over the entire gate range. The mobility is only valid outside the puddle regime and is unphysically high since we assume a vanishing carrier concentration  $n$  at the Dirac point. The high mobility of S1 indicates a good quality of the sample, whereas S2, and S3 can be classified as medium quality samples.

Where we use Eq.(1.43) and the capacitor model 1.40 to calculate the carrier density  $n$ . The constant mobility of S3 follows from its' linear dependence of conductivity on gate voltage. Sample S1 has the highest mobility up to  $14,000 \text{ cm}^2/\text{Vs}$  and therefore represents our best sample. The corresponding mean free path for carrier concentrations larger than puddle concentration ( $n > \alpha Z$ ) $l$  can be calculated by using the Einstein relation:

$$\sigma = \rho(E)e^2 D \quad , \quad D = v_F l \quad (3.2)$$

Here  $D$  is the diffusion constant for a two dimensional system and the DOS  $\rho(E)$  is given by Eq.1.23.

$$l = \frac{\hbar \sigma_{xx}}{e^2} \sqrt{\frac{\pi}{\alpha(V_G - V_D)}} \quad (3.3)$$

The results are shown in Fig.3.5. Since the conductivity is roughly linear in  $V_G - V_D$ , the mean free path will approximately increase with the square root of it. In contrast, for pure short range scatterers, where the conductivity is constant, a decrease would be expected. Our samples lay in a range of 50-100nm (S3) up to 80-180nm (S1). All characterizing parameters are summarized in Tab.3.2

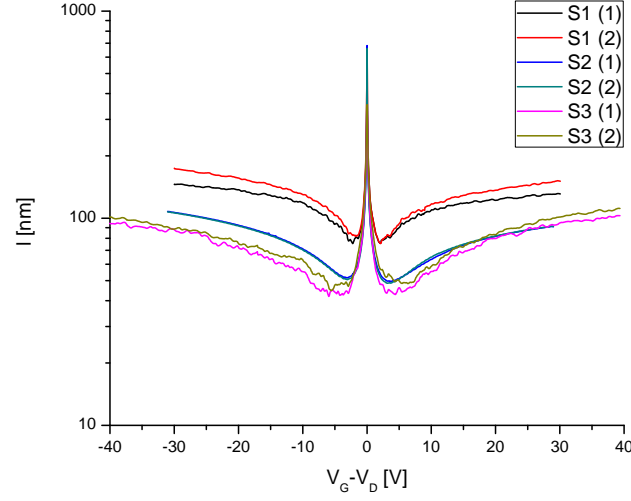


Figure 3.5: Mean free path  $l$  versus back gate voltage. We calculate  $l$  using the Einstein relation for a two-dimensional system. The increasing mean free path indicates the domination of long range scatterers over the gate range.

Table 3.2: Parameters extracted from transport measurement.

sample	$V_D$ [V]	$\mu$ [ $cm^2/Vs$ ]	$l$ [nm]	$Z$ [V]
S1	9	8000 - 14000	80 - 200	0.8
S2	31	5000 - 8000	50 - 120	1
S3	17	4500 - 6000	40 - 100	2

### 3.2 Hall measurement

We use Lock-In amplifiers to measure the voltage drop across the sample. The corresponding resistance is therefore simply obtained by dividing the voltages by the AC current, typically 100nA. However, every measurement of longitudinal resistance  $R_{xx}$  in a Hall bar with invasive, not perfectly aligned contacts will also pick up a transverse component  $\Delta R_{xy}$ . The same is true for measuring the transverse resistance  $R_{xy}$ . It is inevitable to pick up a small longitudinal resistance  $\Delta R_{xx}$ . Since, due to the Onsager relation, the Hall resistance (transverse) is asymmetric in magnetic field  $R_{xy}(-B) = -R_{xy}(B)$ , whereas the longitudinal resistance is symmetric  $R_{xx}(-B) = R_{xx}(B)$ , we can extract the pure  $R_{xx}$  ( $R_{xy}$ ), by adding (subtracting) the measured resistances in opposite magnetic fields and dividing the result by two:

$$R_{even} = \frac{1}{2} [(R_{xx}(B) + \Delta R_{xy}(B)) + (R_{xx}(-B) + \Delta R_{xy}(-B))] = R_{xx} \quad (3.4)$$

$$R_{odd} = \frac{1}{2} [(\Delta R_{xx}(B) + R_{xy}(B)) - (\Delta R_{xx}(-B) + R_{xy}(-B))] = R_H \quad (3.5)$$

The longitudinal resistivity is then obtained by multiplying the resistance with the corresponding aspect ratio, whereas the transverse resistivity and resistance are equivalent for a two dimensional system. We now want to compare the Hall resistances very close to and far away from the current leads. All measurement for S2 and S3 were performed at helium temperature, but for S1 at 100K. This was necessary since one of the three voltage pairs had a bad contact at low temperatures and a direct comparison between the three pairs would not have been possible. The notation for the leads situated very close to the current lead is  $R_{H,\Delta}$ , where  $\Delta$  gives the separation between current and voltage leads in nano meter, whereas for the center leads it is simply  $R_H$ . An optical image of a typical sample is shown in Fig.3.6. Fig.3.8 and Fig.3.7 present the Hall resistances for sample S2 and S3 in low magnetic fields of 0.5, 1, 3T. Both samples give a smaller Hall resistance at  $R_{H,\Delta}$  than at  $R_H$  that in a classical picture simply corresponds to a higher carrier density, since  $R_H \propto n^{-1}$ . Thus our first approach was to explain this by a local doping of the metal leads. However, as discussed in an earlier chapter, depending on the material, graphene would either be electron or hole doped. We see from our multi-band model that any kind of doping results in an decrease of Hall resistance, but also gives raise to a shift in the

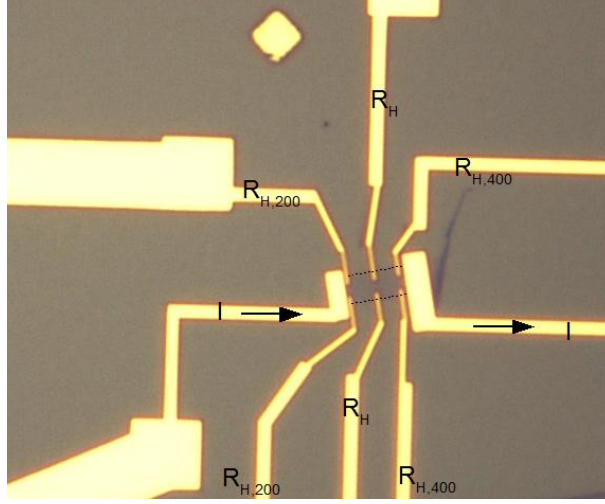


Figure 3.6: Image taken with an optical microscope. The sample has three pairs of voltage leads, where two of them are situated  $200nm$  and  $400nm$  away from the current leads. The sample is about  $6\mu m$  long and  $2.5\mu m$  wide.

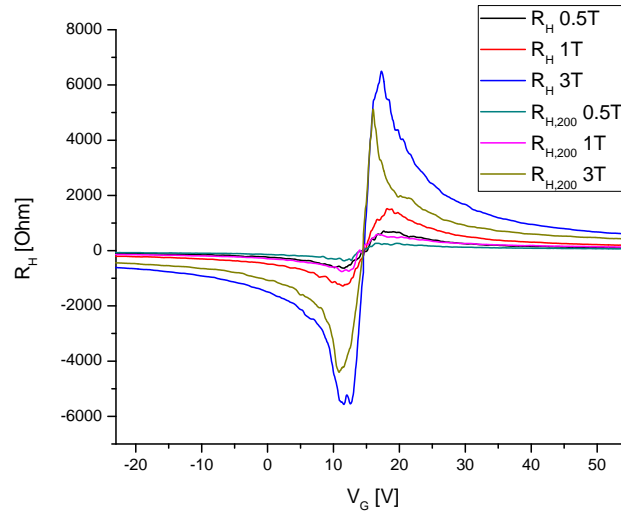


Figure 3.7: Hall resistance  $R_H$  for sample S3. The Hall resistance is increasing in field. The voltage drop at  $R_{H,200}$  is always smaller than in the center of the sample at  $R_H$

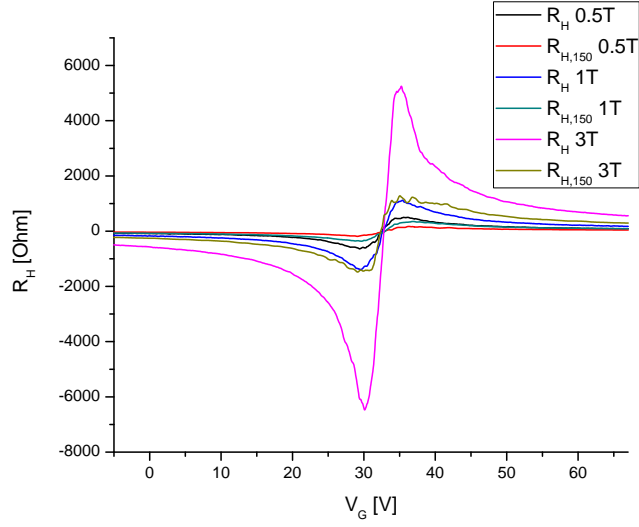


Figure 3.8: Hall resistance  $R_H$  for sample S2. The difference between  $R_{H,150}$  and  $R_H$  is even more pronounced, which indicates the local nature of this effect.

Dirac point. Indeed, there is a small shift ( $\Delta V \leq 0.5V$ ) in the curves of  $R_{H,\Delta}$  to  $R_H$  in both samples, but this can be more likely attributed to small inhomogeneities. Assuming that the carriers mobilities  $f, g$ , the doping concentrations  $c, d$ , and the puddle size  $Z$  is constant throughout the sample, our model fails to explain the smaller resistance at  $R_{H,\Delta}$ . To show that it is at least in general valid (for  $\Delta R_H$ ) we simulate the longitudinal and transverse resistance for S1 in Fig. 3.9. This restricts the value of the fitting parameters. Similar fits can be performed for S2 and S3. It is worth mentioning that all of our fits require a higher value of  $\alpha \approx 8 - 10 * 10^{14} V^{-1} cm^{-2}$  than it is calculated from the simple

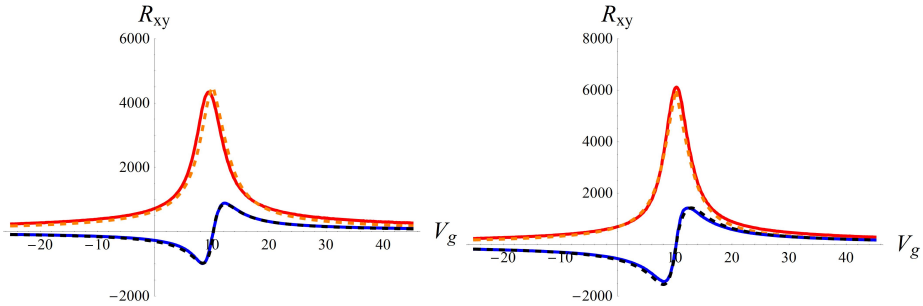


Figure 3.9: Fits for Hall resistance of S1. The dashed curves represent the simulation of the longitudinal and transverse resistances in  $B = 0.5T$  (left) and  $B = 1T$  (right). The fits in one field share all parameters, whereas the mobility and puddle size has to be adjusted for increasing field.

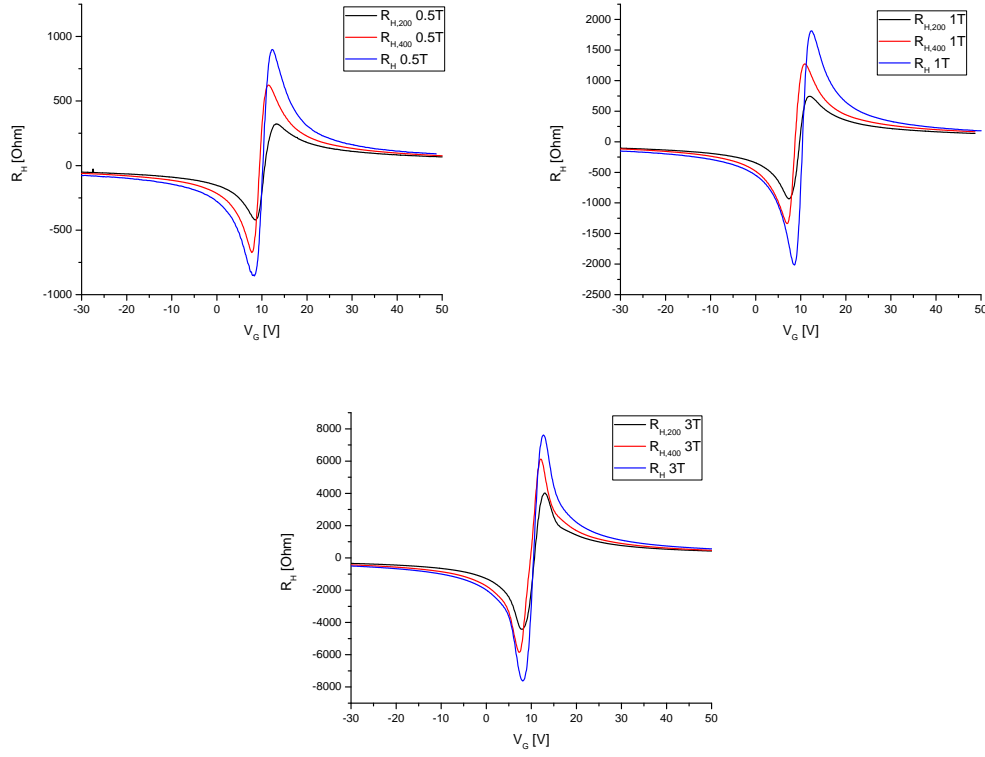


Figure 3.10: Sample S1 in low magnetic field. The voltage drop is decreasing the closer we approach the current lead, but this effect becomes smaller with increasing field. The slight shift of the Dirac point between the curves point might be due to local inhomogeneities and uniform doping through out the sample.

plain capacitor model 1.40. That might be due to edge effects or the general condition of the substrate. We have to increase the puddle size for reasonable fits in higher field, consistent with experiments in Ref.[51]. The mobilities are found to be lower  $f, g \leq 0.05$  than reported in Ref.[36], where the potential fluctuations were not taking into account. In our lowest field of  $0.5T$  we can extract the puddles from the fits to be approximately 0.6, 0.8, 1.2V for S1, S2, S3 respectively, qualitatively consistent with the  $Z$  extracted from the transport measurement in zero field (see Tab.3.2). We see from Fig.3.8 and 3.7 that the discrepancy between the Hall voltages becomes more pronounced when we approach the current lead, but seems to decrease, at least for S2, with raising field. To further investigate this behavior, we designed S1 with an additional, third voltage pair to check the position dependence. We can confirm that the voltage drop at  $R_{H,200}$  is always smaller than at  $R_{H,400}$ , whereas  $R_H$  gives the highest resistance. In addition the change of this effect in

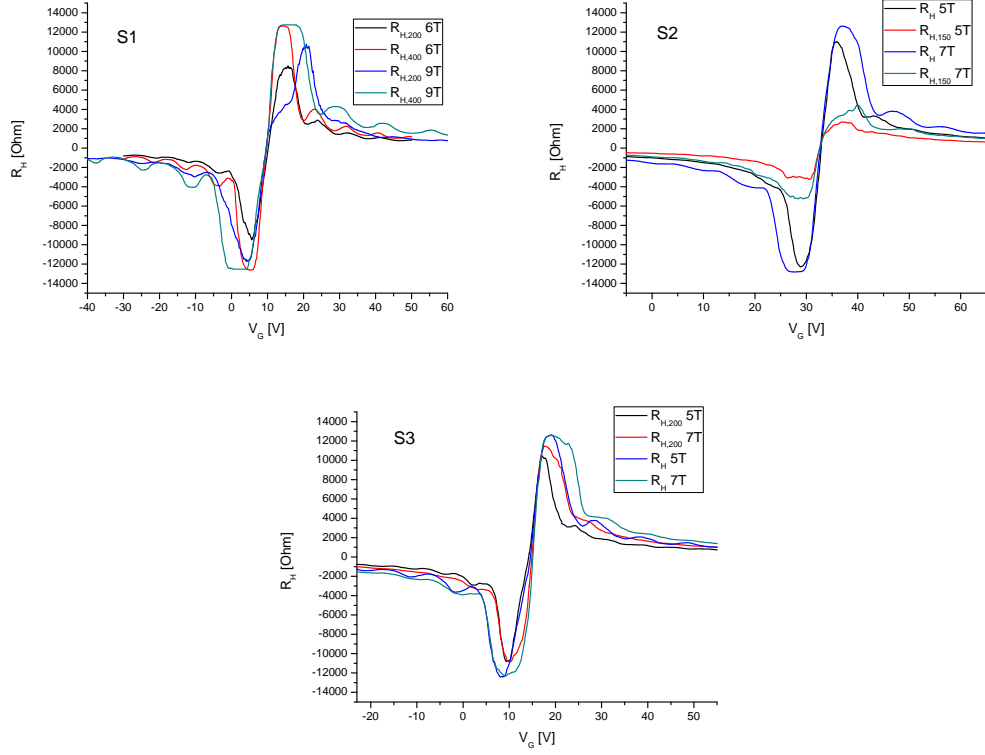


Figure 3.11: Samples in high magnetic fields. All devices show the typical QHE plateaus at  $1/2, 1/6, 1/10 R_K$  for the centered leads  $R_H$ .  $R_{H,400}$  shows also the right quantization, whereas all leads closer than  $400nm$  deviate from the expected value. The strongest deviation is found in S2 where the voltage leads are closest to the current leads.

magnetic field can also be reproduced in S1. This becomes even clearer when we go to high magnetic fields, shown in Fig. 3.11. For S1 and S2 the difference between  $R_{H,\Delta}$  and  $R_H$  is decreasing more and more in magnetic field and  $R_{H,400}$  actually shows the right resistance plateaus in the QH-regime, while  $R_{H,200}$  and especially  $R_{H,200}$  are still underestimating the Hall resistance. The local distribution of this effect thus has to change in magnetic field.

### 3.3 Potential distribution in a Hall bar

Since our model, based on a local doping effect by the metal electrodes, is not appropriate to explain the reduced Hall resistance close to the current leads, we want to introduce a second model. We became aware of some earlier work from the 70's [12] about the potential distribution in Hall bars. Measurements at a  $GaAs - Al_xGa_{1-x}As$  heterostructure were

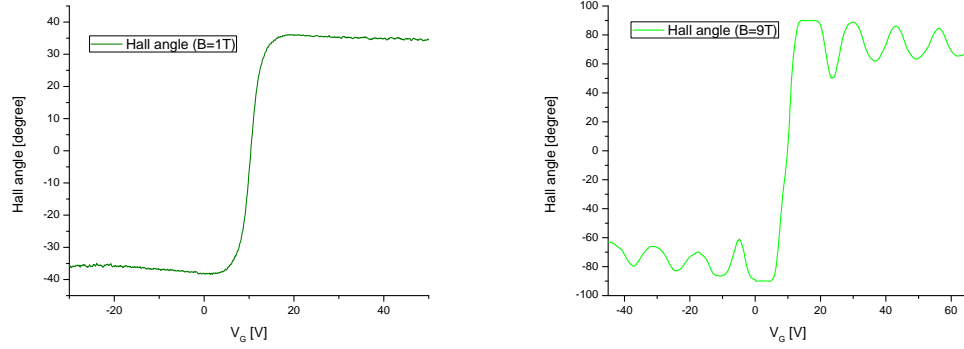


Figure 3.12: Hall angle of S1. Left: In a low field of 1T the Hall angle  $\delta$  is approximately constant in back gate voltage  $V_G$ . Right: In the QH-regime  $\delta$  is oscillating with the filling factor (back gate), due to the SdH-oscillations. At plateaus the Hall angle is ideally  $90^\circ$ s, since the longitudinal resistivity vanishes.

performed 1985 [52] and were in good agreement with the theoretical predictions. The equipotential lines in zero field will ideally be parallel to the current electrodes, since they represent an equipotential, and hence perpendicular to the sample edges. Another boundary condition is given by the current that has to flow parallel at the edge. When a magnetic field is present, the current and field distribution are no longer related by a simple scalar conductivity but by the conductivity tensor 1.42 as discussed above. The current electrodes still impose the boundary condition to be an equipotential, and hence, the distribution of field lines in the channel will not be uniform. One finds that the equipotential distribution depends on the geometry of the sample, width  $W$  and channel length  $L_C$ , and the Hall angle  $\delta = \arctan[\frac{\rho_{xy}}{\rho_{xx}}]$  that is defined by the ratio of the longitudinal to the transverse electric field, and thus by the ratio of transverse to longitudinal resistance (see Eq.1.34). Hence the Hall angle  $\delta$  can be changed by either sweeping the magnetic field or the back gate voltage. For small fields, in the classical Hall effect,  $\delta$  is constant over the gate voltage (see Fig.3.12), but will change sign by sweeping through the Dirac point, while in the QH-regime, where the longitudinal resistance will show Shubnikov de Haas Oscillations [44], it will vary. At the plateaus it is ideally  $90^\circ$  since the longitudinal resistance vanishes, but will change to smaller angles  $\delta \approx 60^\circ - 70^\circ$  when the Fermi level reaches the next Landau level. The equipotential lines for an arbitrary sample shape can be calculated by using the method of conformal mapping [53, 54] with the corresponding boundary condition mentioned above.



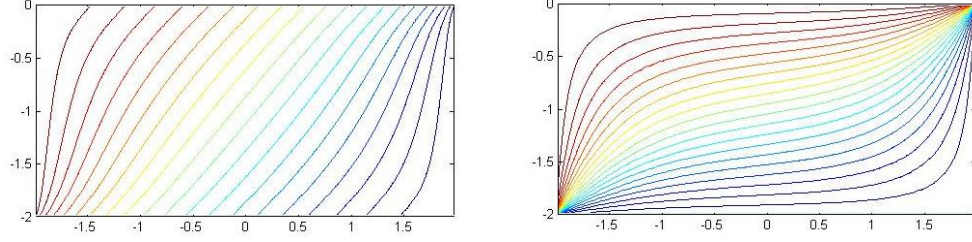


Figure 3.13: Equipotential lines in a Hall Bar. Left: Equipotential lines for  $\frac{\rho_{xy}}{\rho_{xx}} = 1$  ( $\delta = 45^\circ$ ), corresponding to the classical Hall effect in a field of  $B \approx 1T$ . Right: All equipotential lines accumulate in two corners of the samples for Hall angles close to  $90^\circ$ , representing the situation at a QH-plateau.

Fig.3.13 shows equipotential lines for Hall angles of  $\delta = 45$  and  $\delta = 89.9^\circ$ s for a rectangular sample, with an aspect ratio of  $L_C = 2W$  typical for the studied graphene flakes. As the Hall angles increases the equipotential lines get tilted from their parallel alignment to the current leads. They increasingly accumulate at two opposite corners of the Hall bar for higher magnetic fields. Since we can associate the electric field along the channel with the density of the equipotential lines, we see that particularly for large Hall angles the potential will mainly drop in those two corners. The dissipated power per unit area is given by  $\vec{j}\vec{E}$ , where the electric field  $\vec{E}$  and the current density  $\vec{j}$  are related by the resistivity tensor  $\vec{\rho}(\vec{B})$  1.33. It will be close to zero in the interior of the sample for Hall angles of  $\delta \approx 90^\circ$ , since the current and the electric field will be perpendicular to each other. Only at the two corners, where the potential lines accumulate  $\delta$  will always deviate from  $90^\circ$ , even at a Hall plateau, since the current can only flow parallel to the edges. The dissipated power is shown in Fig.3.14, where the absolute value of the electric field is plotted for  $\Delta = 89.5^\circ$ . Due to the dissipation those points are denoted as Hot Spots [55, 12]. They were first observed by measuring the thickness of a helium film on a Hall bar [56] and later by various spectroscopy techniques [51, 57]. At a QH-plateau the entire dissipation will happen in this points and since the voltage drop there will be  $IR_H$  the dissipated power will be  $I^2R_H$ . When the voltage drop  $IR_H = \Delta\mu > \frac{\hbar\omega_c}{2}$  is greater than half of the cyclotron energy, non-equilibrium electrons can be injected from the current leads into excited Landau levels, and then relax by cyclotron emission. This can lead to a local breakdown of the QHE effect [58], due to the non-equilibrium population of Landau levels. The spacing between Landau levels in graphene 1.49, however, is larger than for usual 2DEGs, and a current of  $I = 100nA$

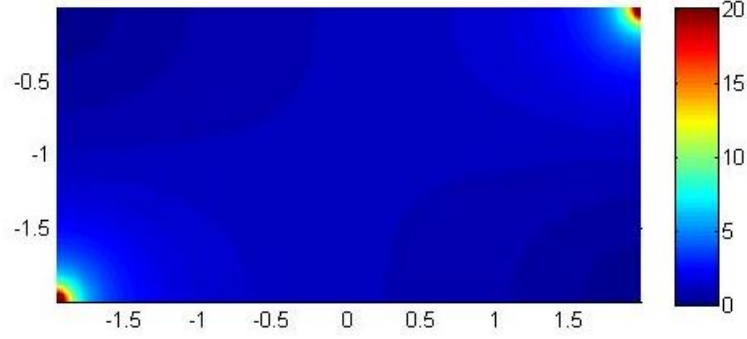


Figure 3.14: Absolute value of electric field in a Hall Bar. This figure shows the absolute value of electric field at a QH-plateau corresponding to the equipotential lines in Fig.3.13 (right). Since the dissipated power is proportional to  $|\vec{E}|^2$  it also shows that most of the power dissipation appears in two corners of the sample.

is about two orders of magnitude smaller than the critical current and the tunneling into higher Landau levels can be ruled out. We will now investigate the effect of the voltage leads on the potential distribution, having in mind the geometry of the leads similar to that of the sample S1. We will distinguish between two scenarios that depend on the contact resistance, and thus on the invasiveness, of the voltage leads.

### 3.3.1 Infinite contact resistance

First we want to consider an infinite contact resistance of the voltage leads. The leads will then be ideally non-invasive, meaning that the potential distribution in the channel will not be affected by them, and they measure the averaged potential of the underlying area. In Fig.3.15 we compare the measured voltage drops at the three Hall voltage pairs. We find, that for small Hall angles (classical Hall effect), the resistance in the center of the sample will be the highest, whereas the closer we approach the current lead the lower it drops. This can explain the deviation of Hall resistances in all samples and the local dependence found in S1, shown in Fig.3.10. With increasing Hall angle the discrepancy between  $R_H$  and  $R_{H,400}$  becomes smaller and will finally vanish at large Hall angles, whereas  $R_{H,200}$  still deviates, since it is situated very close to the Hot Spot. This result is in accordance with the finding, that the deviation between  $R_H$  and  $R_{H,\Delta}$  is decreasing in large magnetic fields. The oscillating Hall angle results in an oscillating deviation between  $R_H$  and  $R_{H,400}$ , that might explain the well pronounced wiggles in  $R_{H,400}$  of S1 in Fig.3.11. This oscillating

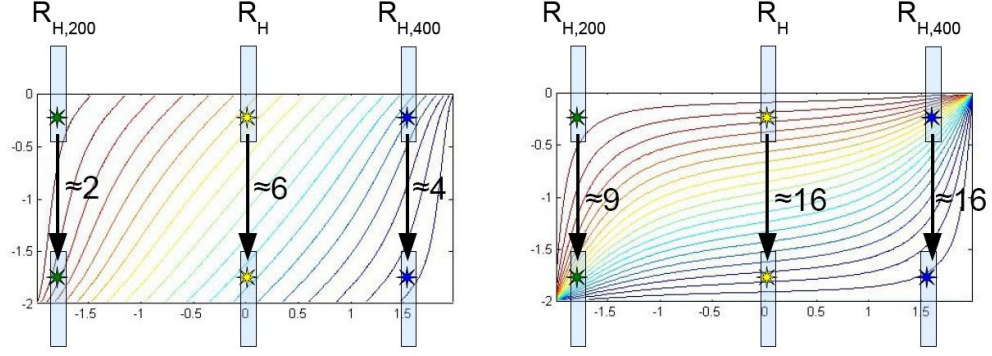


Figure 3.15: Hall measurement with infinite contact resistance of the voltage leads. Current leads are located on the left and right side of the sample, but not shown here. The voltages are given in terms of the corresponding number of equipotentials. The voltage leads average over the underlying lines. Left: Hall angle of  $45^\circ$ . The voltage drop across the sample is partitioned into 20 equal steps. The left side thus corresponds to a chemical potential of 0 whereas the right boundary represents 21. The averaged potential would be smallest for  $R_{H,200}$  and largest for  $R_H$ . Right: For very large angles the center and the right leads would approximately measure the same potential, whereas  $R_{H,200}$  measures a smaller one.

behavior could also be observed in  $R_H$  in a few samples, for example in S2 (and few other samples not presented in this work). That is not surprising since the potential landscape will change there too, and the averaged potential will decrease off QH-plateaus. One way to investigate this issue in future work would be to vary the overlap of the voltage lead with graphene resulting in various amplitudes of those wiggles.

Even though our simple model gives a qualitative understanding of all observed effects, it would clearly underestimate the Hall resistance. In Fig. 3.15, where the potential is divided into 20 equal steps, we would measure a deviation of more than 20% at QH-plateaus. Instead we find in all our samples deviations up to 300 Ohms at the  $\nu = 2$  plateau ( $R_H = 1/2 R_K$ ), so they are much smaller than expected from the model. The reason for that has to be found in the influence of the voltage probes on the channel. Therefore we want to consider the other extreme case, where the contact resistance of the voltage probes vanishes.

### 3.3.2 Vanishing contact resistance

Here we assume that a voltage lead with zero contact resistance will probe only one of the equipotential lines in graphene. At a QH-plateau this would be simply the potential of the edge channel, that is equal to the electrochemical potential of the current lead it

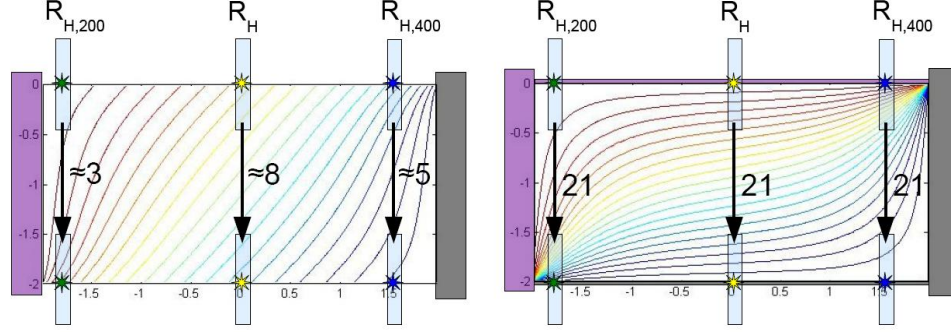


Figure 3.16: Voltage measurement with vanishing contact resistance. For clarity we added the current leads at the left and right side of the channel, having a corresponding chemical potential of 0 and 21. Left: Since the voltage leads have zero contact resistance they will measure the local edge potential (stars) and repel all other lines (not shown here, see Fig. 3.17). The sequence of voltage drops is still the same as for the infinite contact resistance case, but it will be larger in all three pairs. Right: At a QH-plateau all pairs would short out to the edge channel potential and give the right resistance plateau values.

originates from. All other equipotential lines will then be repelled from the lead and we would measure the local potential at this point. As it is shown in Fig. 3.16 there is a potential difference along the sample in the classical regime (for small Hall angles) and  $R_{H,200}$  will still measure the smallest Hall resistance followed by  $R_{H,400}$ . This model would still give us the decreasing deviation between  $R_H$  and  $R_{H,\Delta}$  in high magnetic fields. But as soon as we reach a QH-plateau, where the entire edge channel is at same potential, the model breaks down, since it would predict that all three voltage pairs would probe the same potential, resulting in resistance plateaus. But as we have shown, only  $R_{H,400}$  will reach the value corresponding to QHE, while  $R_{H,200}$  always deviates from the expected value. In particular  $R_{H,150}$  of sample S2 shows the largest discrepancy underlining the strong local nature of this effect. The very fact that we can measure the QHE in our  $R_{H,400}$  lead, indicating a vanishing contact resistance, but not in  $R_{H,200}$ , supporting more the scenario of averaging, suggests, that we have a finite resistance in the leads.

### 3.3.3 Finite contact resistance

From the discussion above we know, that in the classical Hall effect the picture of vanishing contact resistance might be appropriate, since all results can be explained by it. For small Hall angles, the electric fields around each voltage lead, corresponding to a low density of

potential lines, is quite small and we can assume that all voltage probes will repel adjacent equipotential line and give exactly the local edge potential.

For larger Hall angles, however, the equipotential lines are becoming parallel to the edge in most of the sample, and especially at the close voltage leads the local electric field becomes very large, since they are situated close to a Hot Spot. Each voltage lead again imposes the constriction to be an equipotential, but since we have a finite contact resistance in the leads it is not longer necessary that all underlaying equipotential lines are totally repelled. It will then measure a partially averaged potential that can be smaller than the actual edge potential, but larger than the potential measured with a voltage probe with infinite contact resistance. By adopting this model to our potential distribution we are able to reproduce every result.

For the reason of comparison we want to argue that in all samples the  $R_H$  leads give the exact quantized resistances, so we expect that they repel all but one equipotential line. The small deviation that they show becomes immediately clear from the discussion below. And hence the same has to be the case for  $R_{H,400}$ . But why is that not true for  $R_{H,200}$  and  $R_{H,150}$ ? There are two obvious differences between  $R_{H,400}$  and  $R_{H,200}$ . First is the spacing from the current lead, and second, resulting from this and from the existence of the Hot Spot, is the higher density of equipotential lines. Since the current lead inevitable acts as an fixed equipotential, all lines would have to be squeezed to the very small area between the current and voltage leads. This results in an enormous electric field that repels the equipotential lines away from the current leads and forces them under the voltage lead, which then has and measures the averaged potential of the underlying lines. Having said this, it is clear that this effect mainly depends of the location of the voltage lead, but also on its' extent into the graphene, since the number of underlaying potential lines depends on these. Also the contact resistance of the leads might play a crucial role and one would expect even larger deviations for samples contacted with a material of higher contact resistance. Both possibilities should be experimentally provable. The aspect ratio of the sample will be particularly of high importance, since it can be seen in our simulations, that the size of the Hot Spot is increasing with rising width, when the sample length is kept constant. As the dissipation in the Hot Spots depends strongly on the current, it suggests itself to

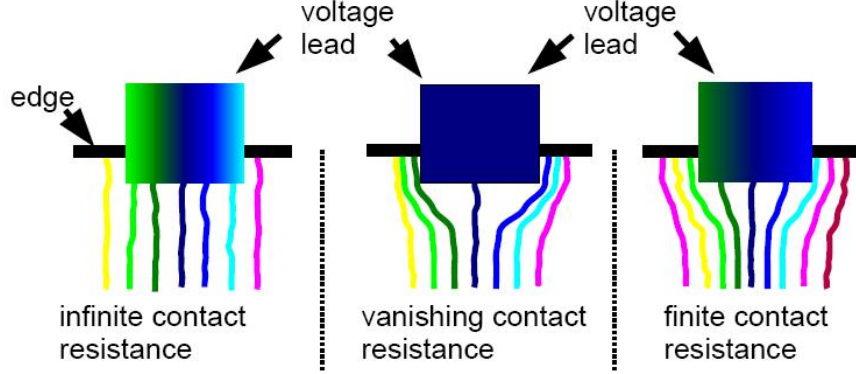


Figure 3.17: Potential distribution for various contact resistances of the voltage leads. This picture shows a very simplified situation of the potential distribution in a rectangular sample in zero field. The potential lines are perpendicular to the sample edge. Left: If the lead has an infinite large contact resistance it will not influence the potential distribution in the sample underneath and measure the averaged potential. Center: The voltage lead will short out to one potential if the contact resistance vanishes, and repel all adjacent lines, since equipotential lines can not cross. It is highly invasive to the potential distribution. Right: If the electric field is too high, not all potential lines can be successfully repelled and the voltage lead will partially average over the potential lines.

In magnetic field, the equipotential lines will get tilted till they eventually are parallel to the edge of the sample at a QH-plateaus. In particularly for large Hall angles, and leads that extend far inside the graphene, this picture becomes very complex and calculations are needed.

investigate the Hall resistance for various currents. Hence higher current densities should lead also to the break down of QHE at  $R_{H,400}$  and lower currents might give the possibility to observe it at  $R_{H,200}$ . A summary of the three scenarios is given in Fig.3.17

The equipotential distributions presented so far represent only one out of four possible configurations, since we can have a positive or negative field, and either electrons or holes as charge carriers. But we can easily apply this model to all other cases, simply because only the Lorentz force on the carriers will change, when we switch the carrier type or the direction of the field. The Hot Spots would then jump from the lower left and upper right corner to the upper left and lower right corner. As only the lower left  $R_{H,200}$  voltage probe in Fig.3.16 is affected by the Hot Spots we can expect an asymmetry between the longitudinal resistances  $\rho_{xx}$  of the upper and lower edge in the QH-regime. This is shown in Fig.3.18 for sample S1. The resistivity  $\rho_{1,2}$  at the Hall plateaus at the upper edge is vanishing only on the electron side ( $V_G > V_D$ ) in negative field ( $B = -9T$ ) and at the hole side ( $V_G < V_D$ )

in positive field ( $B = 9T$ ). The situation for the resistivity  $\rho_{3,4}$  is just the opposite. And as expected from the discussion above,  $\rho_{1,2}$  in a negative (positive) field is indeed equal to  $\rho_{3,4}$  in a positive (negative field), indicating a jump of the Hot Spots to the other two corners upon reversal of the magnetic field. The symmetry between electrons in a positive field and holes in negative field, and vice versa, can also be seen. However it is not as well pronounced as the symmetry in opposite edges for reversed fields, that might be explained by different scattering mechanisms for different carrier types.

### 3.3.4 Summary and Outlook

Starting from the idea of a local doping effect by the current electrodes, we developed a multi-band model to simulate the Hall resistance for doped graphene. We could successfully reproduce the Hall resistances in the center of the sample by limiting the disorder to two type of dopants occupying acceptor levels far away from and very close to the Dirac point. However we did not observe a local doping effect when using titanium/gold electrodes. Since we have used a very thin layer of titanium that may not wet graphene uniformly, it is possible, that the doping by titanium and gold almost cancel each other and the local doping effect eventually vanishes. A further investigation of this issue is still needed and a suitable material would be aluminum, since the work function difference between aluminum and graphene is huge, and the doping should then be more pronounced.

As our model could not give satisfactory agreement with finding that the Hall resistance close to the current leads is too low, we developed a model based on the potential distribution in the Hall bar. Assuming a finite contact resistance in our voltage probes we find, that for probing the QHE it is essential that the voltage leads are situated reasonably far from the Hot Spots, which necessarily occur for large Hall angles. But in addition to the spacing between voltage and current lead, the extent of the Hall probes into graphene, the aspect ratio of the sample, and particularly the applied current might be crucial. We also expect that the invasiveness of the electrodes is determined by the contact resistance and thus changes for different material.

However all our assumptions are based on equipotential calculation for a perfectly rectangular sample, not taking into account any voltage leads. Every metal probe will represent

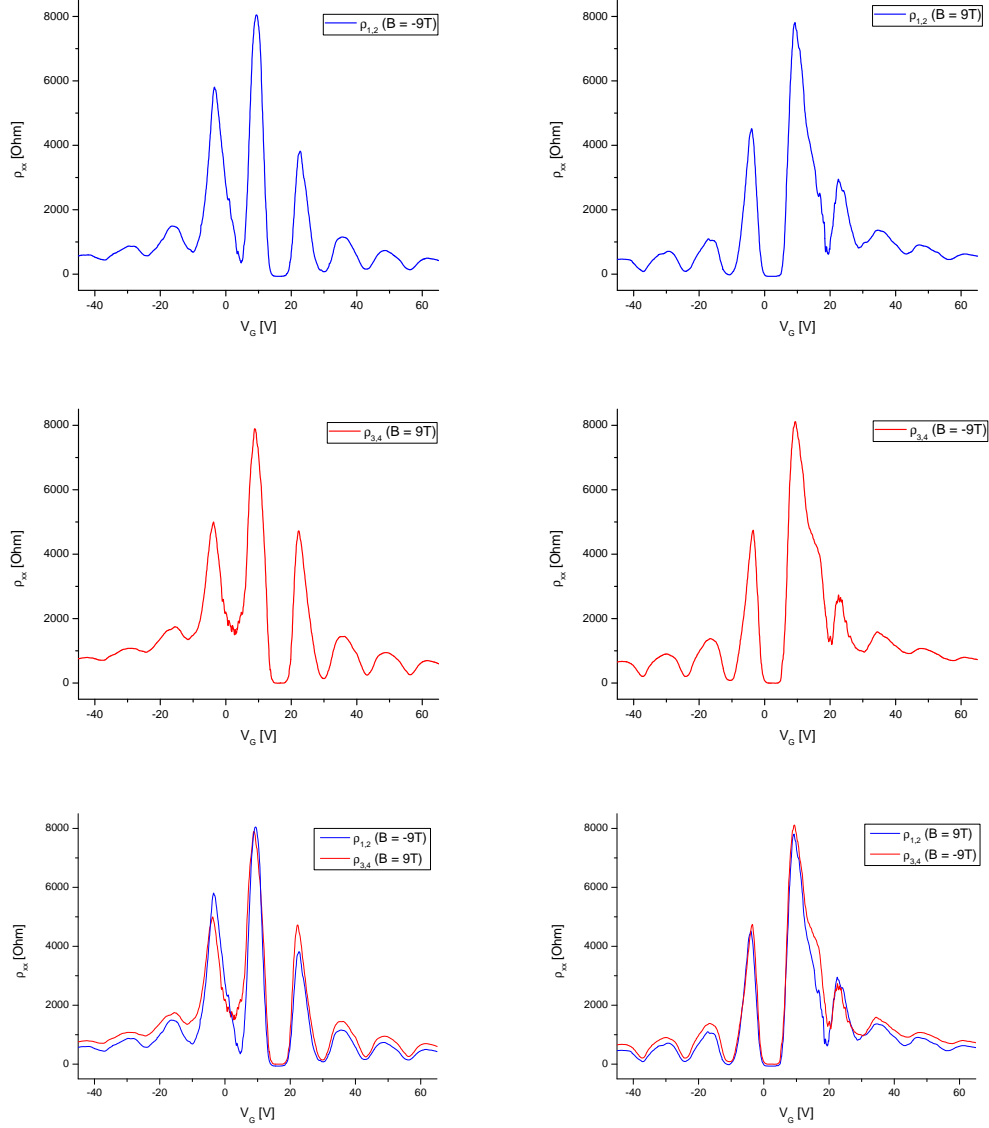


Figure 3.18: Longitudinal resistance of S1 in 9 Tesla. We find that  $\rho_{xx}$  shows an asymmetry in field, carrier type and edge. Reversing magnetic field has the same effect as measuring longitudinal resistivity at the other edge. This can be explained by the existence of hot spots at two diagonal corners of the sample (see Fig.3.14) that will jump to the vertically opposite corners when the field or carrier type is reversed (see text).



an equipotential and thus imposes additional boundary conditions to the problem. Better calculations considering the invasiveness of the leads, depending on their contact resistance, are thus needed. By all means it is advisable to use external voltage probes to avoid those problems. The patterning of graphene into Hall bars by plasma etching followed by contacting it by external probes is a common technique, but so far no patterned suspended sample has been reported. The size of those samples is usually in the order of more than  $5\mu m$  and it will be an engineering challenge to suspend such a large sample. The problems of power dissipation caused by the Hot Spots might be even more important in suspended graphene, since it provides higher mobilities, leading to a spreading of the dissipation to a larger area. In addition it has no underlying substrate where the heat could dissipate, that might further intensify this issue. The very fact that in our suspended Hall bar the Hall resistance was much smaller than expected for QHE justifies this assumption.

The back door to observe the QHE even in suspended graphene is to use a simple two lead measurement, where the voltage drop is directly measured at the current leads. In this configuration we were not only able to measure the QHE in suspended graphene for the first time, but also the fractional QHE<sup>1</sup>.

---

<sup>1</sup>both papers in print

## References

- [1] K. S. Novoselov, A. K. Geim, S. V. Morozov, D. Jiang, Y. Zhang, S. V. Dubonos, I. V. Grigorieva, and A. A. Firsov, “Electric Field Effect in Atomically Thin Carbon Films,” *Science* **306** (2004), no. 5696, 666–669, [arXiv](#) <http://www.sciencemag.org/cgi/reprint/306/5696/666.pdf>.
- [2] N. D. Mermin, “Crystalline order in two dimensions,” *Phys. Rev.* **176** (Dec, 1968) 250–254.
- [3] C. Lee, X. Wei, J. W. Kysar, and J. Hone, “Measurement of the elastic properties and intrinsic strength of monolayer graphene,” *Science* **321** (July, 2008).
- [4] F. Schedin, A. K. Geim, S. V. Morozov, E. W. Hill, P. Blake, M. I. Katsnelson, and K. S. Novoselov, “Detection of individual gas molecules adsorbed on graphene,” *Nature Materials* **6** (Sept., 2007) 652–655.
- [5] A. K. Geim, “Graphene: Status and Prospects,” *Science* **324** (2009), no. 5934, 1530–1534, [arXiv](#) <http://www.sciencemag.org/cgi/reprint/324/5934/1530.pdf>.
- [6] A. H. C. Neto, F. Guinea, N. M. R. Peres, K. S. Novoselov, and A. K. Geim, “The electronic properties of graphene,” *Reviews of Modern Physics* **81** (2009), no. 1, 109.
- [7] K. V. Klitzing, G. Dorda, and M. Pepper, “New Method for High-Accuracy Determination of the Fine-Structure Constant Based on Quantized Hall Resistance,” *Physical Review Letters* (1980).
- [8] K. S. Novoselov, A. K. Geim, S. V. Morozov, D. Jiang, M. I. Katsnelson, I. V. Grigorieva, S. V. Dubonos, and A. A. Firsov, “Two-dimensional gas of massless dirac fermions in graphene,” *Nature Physics* **438** (Nov., 2005) 197–200, [arXiv](#) [arXiv:cond-mat/0509330](http://arxiv.org/abs/cond-mat/0509330).
- [9] X. Du, I. Skachko, A. Barker, and E. Y. Andrei, “Approaching ballistic transport in suspended graphene,” *Nature Nanotechnology* **3** (Aug., 2008) 491–495, [arXiv](#) [0802.2933](http://arxiv.org/abs/0802.2933).
- [10] K. I. Bolotin, K. J. Sikes, Z. Jiang, M. Klima, G. Fudenberg, J. Hone, P. Kim, and H. L. Stormer, “Ultrahigh electron mobility in suspended graphene,” *Solid State Communications* **146** (2008) 351.
- [11] G. Giovannetti, P. A. Khomyakov, G. Brocks, V. M. Karpan, J. van den Brink, and P. J. Kelly, “Doping graphene with metal contacts,” *Physical Review Letters* **101** (2008), no. 2, 026803.
- [12] J. ichi Wakabayashi and S. Kawaji, “Hall effect in silicon mos inversion layers under strong magnetic fields,” *Journal of the Physical Society of Japan* **44** (1978), no. 6, 1839–1849.

- [13] U. Klaß, W. Dietsche, K. Klitzing, and K. Ploog, “Imaging of the dissipation in quantum-Hall-effect experiments,” *Zeitschrift für Physik B Condensed Matter* **82** (Oct., 1991) 351–354.
- [14] P. R. Wallace, “The band theory of graphite,” *Phys. Rev.* **71** (May, 1947) 622–634.
- [15] G. R. Saito and M. Dresselhaus, *Physical properties of carbon nanotubes*. Imperial College Press, 1996.
- [16] S. Reich, J. Maultzsch, C. Thomsen, and P. Ordejón, “Tight-binding description of graphene,” *Phys. Rev. B* **66** (Jul, 2002) 035412.
- [17] R. Shankar, *Principles of Quantum mechanics*. Springer, 2009.
- [18] P. e. a. Kim, “Experimental observation of the quantum hall effect and berry’s phase in graphene,” *Nature* (2005).
- [19] G. P. Mikitik and Y. V. Sharlai, “Manifestation of berry’s phase in metal physics,” *Phys. Rev. Lett.* **82** (Mar, 1999) 2147–2150.
- [20] T. Ando, T. Nakanishi, and R. Saito, “Berry’s phase and absence of back scattering in carbon nanotubes,” *Journal of the Physical Society of Japan* **67** (Aug., 1998) 2857–+.
- [21] J. Martin, N. Akerman, G. Ulbricht, T. Lohmann, J. H. Smet, K. von Klitzing, and A. Yacoby, “Observation of electron-hole puddles in graphene using a scanning single-electron transistor,” *Nature Physics* **4** (Feb., 2008) 144–148, [arXiv 0705.2180](#).
- [22] E. Rossi, S. Adam, and S. Das Sarma, “Effective medium theory for disordered two-dimensional graphene,” *Phys. Rev. Lett. B* **79** (June, 2009) 245423–+, [arXiv 0809.1425](#).
- [23] N. M. R. Peres, F. Guinea, and A. H. C. Neto, “Electronic properties of disordered two-dimensional carbon,” *Physical Review B (Condensed Matter and Materials Physics)* **73** (2006), no. 12, 125411.
- [24] K. Nomura and A. H. MacDonald, “Quantum transport of massless dirac fermions,” *Physical Review Letters* **98** (2007), no. 7, 076602.
- [25] L. Falkovsky and A. Varlamov, “Space-time dispersion of graphene conductivity,” *Eur. Phys. J. B* **56** (apr, 2007) 281–284.
- [26] T. Stauber, N. M. R. Peres, and A. H. C. Neto, “Conductivity of suspended and non-suspended graphene at finite gate voltage,” *Physical Review B* **78** (2008) 085418.
- [27] P. Blake, R. Yang, S. Morozov, F. Schedin, L. Ponomarenko, A. Zhukov, R. Nair, I. Grigorieva, K. Novoselov, and A. Geim, “Influence of metal contacts and charge inhomogeneity on transport properties of graphene near the neutrality point,” *Solid State Communications* **149** (2009), no. 27-28, 1068 – 1071. Recent Progress in Graphene Studies.
- [28] S. Adam, E. Hwang, and S. D. Sarma, “Scattering mechanisms and boltzmann transport in graphene,” *Physica E: Low-dimensional Systems and Nanostructures* **40** (2008), no. 5, 1022 – 1025. 17th International Conference on Electronic Properties of Two-Dimensional Systems.

- [29] M. Trushin and J. Schliemann, “Conductivity of graphene: How to distinguish between samples with short- and long-range scatterers,” *EPL (Europhysics Letters)* **83** (2008), no. 1, 17001 (6pp).
- [30] D. S. Novikov, “Numbers of donors and acceptors from transport measurements in graphene,” *Applied Physics Letters* **91** (Sept., 2007) 102102–+, [arXiv 0707.1106](#).
- [31] J.-H. Chen, C. Jang, S. Adam, M. S. Fuhrer, E. D. Williams, and M. Ishigami, “Charged-impurity scattering in graphene,” *Nature Physics* **4** (May, 2008) 377–381, [arXiv 0708.2408](#).
- [32] E. J. H. Lee, K. Balasubramanian, R. T. Weitz, M. Burghard, and K. Kern, “Contact and edge effects in graphene devices,” *Nature Nanotechnology* **3** (Aug., 2008) 486–490.
- [33] R. Golizadeh-Mojarad and S. Datta, “Effect of contact induced states on minimum conductivity in graphene,” *Physical Review B (Condensed Matter and Materials Physics)* **79** (2009), no. 8, 085410.
- [34] B. Huard, N. Stander, J. A. Sulpizio, and D. Goldhaber-Gordon, “Evidence of the role of contacts on the observed electron-hole asymmetry in graphene,” *Physical Review B (Condensed Matter and Materials Physics)* **78** (2008), no. 12, 121402.
- [35] A. S., “On a new Action of the Magnet on Electric Currents,” *Nature* **21** (Feb., 1880) 361–+.
- [36] T. O. Wehling, K. S. Novoselov, S. V. Morozov, E. E. Vdovin, M. I. Katsnelson, A. K. Geim, and A. I. Lichtenstein, “Molecular doping of graphene,” *Nano Letters* **8** (2008), no. 1, 173–177, [% tt arXiv http://pubs.acs.org/doi/pdf/10.1021/nl072364w](#).
- [37] G. Grosso, *Solid State Physics*. Academic Press, 2000.
- [38] J. W. McClure, “Diamagnetism of graphite,” *Phys. Rev.* **104** (Nov, 1956) 666–671.
- [39] K. S. Novoselov, Z. Jiang, Y. Zhang, S. V. Morozov, H. L. Stormer, U. Zeitler, J. C. Maan, G. S. Boebinger, P. Kim, and A. K. Geim, “Room-Temperature Quantum Hall Effect in Graphene,” *Science* (2007) 1137201.
- [40] F. Delahaye and D. Bornaud, “Low-noise measurements of the quantized hall resistance using an improved cryogenic current comparator bridge,”.
- [41] K. S. Novoselov, E. McCann, S. V. Morozov, V. I. Falko, M. I. Katsnelson, U. Zeitler, D. Jiang, F. Schedin, and A. K. Geim, “Unconventional quantum hall effect and berry’s phase of  $2\pi$  in bilayer graphene,” *Nature Physics* (2006).
- [42] M. Büttiker, “Absence of backscattering in the quantum hall effect in multiprobe conductors,” *Phys. Rev. B* **38** (Nov, 1988) 9375–9389.
- [43] L. R., “Electrical resistance of disordered one-dimensional lattices,” *Phil. Mag.*
- [44] L. S. . W. J. D. HAAS, “A new phenomenon in the change of resistance in a magnetic field of single crystals of bismuth,” *Nature* **126** (1930), no. 500,.
- [45] M. Sze, *Physics of Semiconductor Devices*. Wiley, 2006.

- [46] Z. Cui, *Nanofabrication: Principles, Capabilities and Limits*. Springer, 2008.
- [47] R. W. Johnstone, I. G. Foulds, M. V. Pallapa, and A. M. Parameswaran, “Isopropanol/water as a developer for poly(dimethylglutarimide),” *Journal of Micro/Nanolithography, MEMS and MOEMS* **7** (2008), no. 4, 043006.
- [48] Wajid, Abdul (East Syracuse, NY), *Measuring and controlling deposition on a piezoelectric monitor crystal*. No. 5112642. May, 1992.
- [49] S. V. Morozov, K. S. Novoselov, M. I. Katsnelson, F. Schedin, D. C. Elias, J. A. Jaszczak, and A. K. Geim, “Giant intrinsic carrier mobilities in graphene and its bilayer,” *Physical Review Letters* **100** (2008), no. 1, 016602.
- [50] E. H. Hwang, S. Adam, and S. D. Sarma, “Carrier transport in two-dimensional graphene layers,” *Physical Review Letters* **98** (2007), no. 18, 186806.
- [51] K. Ikushima, H. Sakuma, S. Komiyama, and K. Hirakawa, “Imaging of Cyclotron Emission from Edge Channels in Quantum Hall Conductors,” *Physical Review Letters* **93** (Sept., 2004) 146804–+.
- [52] E. K. Sichel, H. H. Sample, and J. P. Salerno, “Equipotential distribution in the quantum hall effect,” *Phys. Rev. B* **32** (Nov, 1985) 6975–6977.
- [53] R. F. Wick, “Solution of the field problem of the germanium gyrator,” *Journal of Applied Physics* **25** (1954), no. 6, 741–756.
- [54] D. A. Abanin and L. S. Levitov, “Conformal invariance and shape-dependent conductance of graphene samples,” *Physical Review B (Condensed Matter and Materials Physics)* **78** (2008), no. 3, 035416.
- [55] U. Klaß, W. Dietsche, K. Klitzing, and K. Ploog, “Imaging of the dissipation in quantum-Hall-effect experiments,” *Zeitschrift für Physik B Condensed Matter* **82** (Oct., 1991) 351–354.
- [56] U. Klaß, W. Dietsche, K. Klitzing, and K. Ploog, “Imaging of the dissipation in quantum-Hall-effect experiments,” *Zeitschrift für Physik B Condensed Matter* **82** (Oct., 1991) 351–354.
- [57] H. Sakuma, K. Ikushima, S. Komiyama, and K. Hirakawa, “Spectroscopy of non-equilibrium electrons in quantum hall conductors,” *Physica E: Low-dimensional Systems and Nanostructures* **34** (2006), no. 1-2, 168 – 171. Proceedings of the 16th International Conference on Electronic Properties of Two-Dimensional Systems (EP2DS-16).
- [58] Y. Kawano and S. Komiyama, “Local breakdown of the quantum hall effect and the correlated cyclotron emission,” *Physica E Low-Dimensional Systems and Nanostructures* **7** (May, 2000) 799–803.